J. Mech. Phys. Solids 191 (2024) 105771

Contents lists available at ScienceDirect

Journal of the Mechanics and Physics of Solids

journal homepage: www.elsevier.com/locate/jmps

Deformation, shape transformations, and stability of elastic rod loops within spherical confinement

Meng Wang, Xiying Li, Xin Yi *

State Key Laboratory for Turbulence and Complex System, Department of Mechanics and Engineering Science, College of Engineering, Peking University, Beijing 100871, China

ARTICLE INFO

Keywords:
Thin elastic rods
Confinement
Packing
Stability analysis
Euler rotation curves
Inhomogeneity

ABSTRACT

Mechanical insight into the packing of slender objects within confinement is essential for understanding how polymers, filaments, or wires organize and rearrange in limited space. Here we combine theoretical modeling, numerical optimization, and experimental studies to reveal spherical packing behavior of thin elastic rod loops of homogeneous or inhomogeneous stiffness. Across varying loop lengths, a rich array of configurations including circle, saddle, figure-eight, and more intricate patterns are identified. A theoretical framework rooted in the local equilibrium of force and moment is proposed for the rod loop deformation, facilitating the determination of internal and contact forces experienced by the rods during deformation. For the confined homogeneous rod loops, their stable and metastable configurations are well described using proposed Euler rotation curves, which offer a concise and effective approach for configuration prediction. Moreover, formulated analysis on the stability and critical force for homogeneous rod loops on great circles of the spherical confinement are performed. For inhomogeneous rod loops with two segments of differing stiffness, the stiffer segment exhibits less deviation from the great circle, while the softer segment undergoes more pronounced deformation. These findings not only enhance our understanding of buckling and post-buckling phenomena but also offer insights into filament patterning within confining environments.

1. Introduction

Geometrical confinement, arising from physical boundaries such as walls, membranes, and fluid interfaces, generally imposes geometric incompatibility for confined objects undergoing complex spatial rearrangements. Understanding how surface confinement shapes filamentary objects is not only of fundamental interest but also holds relevance for a multitude of biological, medical, and industrial applications spanning various length scales. Microscale examples include DNA packaging in viral capsids and bacterial envelopes (Purohit et al., 2003; Coshic et al., 2024), as well as the organization of actin filaments within vesicles, droplets, and cell-sized confinement (Limozin and Sackmann, 2002; Jiang and Sun, 2010; Diagouraga et al., 2014; Tsai and Koenderink, 2015; Shi et al., 2023; Graham et al., 2024). At larger length scales, primary examples encompass fiber coiling in or around droplets (Chen and Zhang, 2022; Sannyamath et al., 2024), ordered and disordered packing of wires in cavities or flexible confinement (Stoop et al., 2011; Vetter et al., 2014; Shaebani et al., 2017; Lombardo et al., 2018), guidewire navigation in endovascular surgery, and buckling of fibers embedded in a matrix (Slesarenko and Rudykh, 2017; Huang et al., 2024).

In the realm of the aforementioned examples, investigations into spherical confinement hold paramount significance. Firstly, this significance stems from the fact that structures such as droplet surfaces, cell membranes, and viral capsids impose a form of

* Corresponding author.
E-mail address: xyi@pku.edu.cn (X. Yi).

https://doi.org/10.1016/j.jmps.2024.105771
Received 14 May 2024; Received in revised form 24 June 2024; Accepted 4 July 2024
Available online 8 July 2024

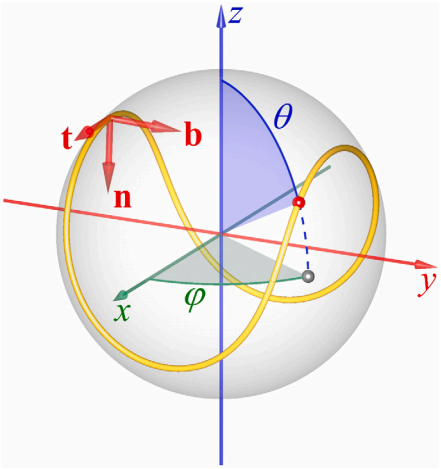

Fig. 1. Schematic of an inextensible rod loop of total length L confined within a rigid spherical confinement of radius R. In a spherical coordinate system with its origin located at the center of the spherical confinement, every rod curve point has spherical coordinates (ρ, θ, φ) with radial distance $\rho(\leq R)$, polar angle θ, and azimuthal angle φ. Along the rod curve, the Frenet–Serret frame $\{\mathbf{t}, \mathbf{n}, \mathbf{b}\}$ is defined, where the vectors $\mathbf{t}$, $\mathbf{n}$, and $\mathbf{b}$ represent the unit tangent, unit principal normal, and unit binormal vectors, respectively. The arclength s is measured in the direction of $\mathbf{t}$.

confinement that approximates a spherical shape. Secondly, the sphere's inherent high degree of symmetry plays an essential role in simplifying numerous geometric problems, thus establishing it as a cornerstone for comprehending spatial relationships.

In this work, we delve into the packing of thin elastic rod loops in spheres, with a particular focus on rod deformation, shape transformations, and stability. Modeling the spherical surface-constrained rod loops as closed elastic curves, early theoretical investigations on this subject garnered attention primarily from a mathematical perspective. For example, pioneering studies employed variational techniques, both with and without constraints on curve length, yielding governing equations of curvature, torsion, and geodesic curvature of these constrained elastic curves (Langer and Singer, 1984; Brunnett and Crouch, 1994; Arroyo et al., 2006). At specified values of the Lagrange multiplier associated with the constrained curve length, wavelike, orbitlike, and borderline curve profiles were unveiled (Langer and Singer, 1984; Brunnett and Crouch, 1994; Arroyo et al., 2006). Effects of intrinsic curvature of the elastic curves have also been analyzed (Arroyo et al., 2006). While these studies primarily emphasized mathematical variations and geometry, the mechanical interaction between the elastic curve and the confining surface received less attention. More recently, the surface confinement constraint has been incorporated into variational frameworks to explore transmitted forces arising from rod-surface contact (Guven and Vázquez-Montejo, 2012; Huynen et al., 2016). However, these frameworks predominantly yield complex mathematical solutions rather than comprehensive mechanical treatments, limiting their utility for engineers and practical applications. Additionally, the effect of rod inhomogeneity on packing remains unexplored. Moreover, despite theoretical advancements, experimental demonstrations on the packing of elastic loops within spheres are lacking. There exists a pressing need for theoretically derived, mechanically grounded approaches to predict the deformation of slender rod loops confined within spherical enclosures. Such approaches not only offer insights into theoretical mechanisms but also serve as a valuable resource for practical applications.

In the present study, we gain mechanical insight into the packing of elastic rod loops within spherical confinement. After introducing theoretical modeling and numerical methods in Section 2, a diverse spectrum of stable and metastable configurations of the confined homogeneous rod loops are elucidated theoretically and experimentally in Section 3, displaying a wide variety of symmetries as the relative length of the rod varies. Predictions on the rod configurations are carried out based on the Euler rotation curve approximation proposed in Section 3 and analytical solutions derived from local equilibrium equations in Section 4. Stability and force analysis for homogeneous rod loops on great circles are also performed. Section 5 examines the effects of rod inhomogeneity on packing. Finally, Sections 6 and 7 offer further discussion and conclude the study.

2. Theoretical modeling and numerical methods

Consider an inextensible thin elastic prismatic rod loop confined within a rigid spherical confinement of radius R, and frictionless contact between the rod and the confinement is assumed. The thin rod of total length $L(\geq 2\pi R)$ and bending stiffness D has the same circular cross section along its centerline. Here $D = EI$ with E as the Young's modulus and I as the moment of inertia of the circular cross section. In the adopted spherical coordinate system (Fig. 1), the equilibrium configuration of the confined rod is characterized via the centerline, modeled as an arclength parameterized space curve of position vector

$$\mathbf{r}(s) = \rho(s)\sin\theta(s)\cos\varphi(s)\mathbf{e}_x + \rho(s)\sin\theta(s)\sin\varphi(s)\mathbf{e}_y + \rho(s)\cos\theta(s)\mathbf{e}_z, \tag{1}$$

where s is the arclength, (ρ, θ, φ) denotes the spherical coordinates of the curve point at $\mathbf{r}(s)$ with $\rho(s)$ as the radial distance, $\theta(s)$ the polar angle, and $\varphi(s)$ the azimuthal angle, and $\mathbf{e}_x$, $\mathbf{e}_y$, and $\mathbf{e}_z$ denote unit vectors along the $x-$, $y-$, and $z-$ axes of a Cartesian

coordinate system sharing the same origin with the spherical coordinate system. In our analysis, the reference point for $s = 0$ is defined as an arbitrarily selected point of contact between the confined rod and the sphere inner surface. Inextensible constraint of the rod requires $|\mathbf{r}'(s)| = 1$, where the prime represents derivative with respect to the arclength s hereinafter (e.g., $\mathbf{r}''(s) = \mathrm{d}^2\mathbf{r}/\mathrm{d}s^2$). For an inhomogeneous rod, the Young's modulus E could vary along the centerline and one has $D = D(s)$.

The continuity and smoothness of the rod loop require continuities of $\mathbf{r}$ and tangent vector $\mathbf{t}(= \mathbf{r}')$. Meanwhile, in the free and contact portions of the rod, the function $\mathbf{r}(s)$ is assumed to have four continuous derivatives $\mathbf{r}^{(i)}(s)$ $(i = 1, 2, 3, 4)$ to ensure the continuities of the curvature, torsion, bending moment, contact force, and internal forces.

Adopting the wormlike chain model for the thin elastic rod (Kratky and Porod, 1949; Doi and Edwards, 1986), the elastic energy E_{el} of the system is the pure bending energy with the twist energy neglected and is given by

$$E_{\mathrm{el}} = \frac{1}{2}\int_0^L D\kappa^2 \mathrm{d}s, \tag{2}$$

where $\kappa(s) = |\mathbf{r}''(s)|$ is the local curvature of the rod centerline.

In numerical studies, the spherical coordinate functions $\rho(s)$, $\theta(s)$, and $\varphi(s)$ are approximated using sextic B-spline functions as $\rho(s) = \sum_{j=1}^{n} a_j N_j(s)$, $\theta(s) = \sum_{j=1}^{n} b_j N_j(s)$, and $\varphi(s) = \sum_{j=1}^{n} c_j N_j(s)$, where a_j, b_j, and c_j are coefficients of basis functions $N_j(s)$ defined recursively on a uniform knot vector of s. The polynomial functions $N_j(s)$ can be derived by means of the Cox–de Boor recursion formula (Farin, 2002). Through the geometric relationship in Eq. (1), the elastic deformation energy E_{el} in Eq. (2) at a given rod length L becomes $E_{\mathrm{el}} = E_{\mathrm{el}}(a_j, b_j, c_j)$ as a function of the undetermined coefficients a_j, b_j, and c_j. Here, a_j, b_j, and c_j are not independent and are required to satisfy the local inextensible constraint of the rod $|\mathbf{r}'(s)| = 1$, which preserves $\mathrm{d}s$ as the local arclength element. Additionally, the spherical confinement imposes $0 < \rho(s) \le R$. The closure conditions of the rod loop read

$$\mathbf{r}(0) = \mathbf{r}(L) = R\mathbf{e}_x \quad \text{and} \quad \mathbf{r}^{(i)}(0) = \mathbf{r}^{(i)}(L) \quad (i = 1, 2, 3, 4). \tag{3}$$

Eq. (3) leads to $\rho(0) = \rho(L) = R$, $\rho^{(i)}(0) = \rho^{(i)}(L)$, $\theta(0) = \theta(L)$, $\theta^{(i)}(0) = \theta^{(i)}(L)$, $\varphi(L) - \varphi(0) = 2\pi p$ with p as an integer, and $\varphi^{(i)}(0) = \varphi^{(i)}(L)$. These requirements provide input parameters and equality or inequality constraints in the numerical optimization.

Given the energy function $E_{\mathrm{el}} = E_{\mathrm{el}}(a_j, b_j, c_j)$ and its first derivatives with respect to the coefficients a_j, b_j, and c_j, the minimum energy E_{el} at a given rod length L and the corresponding values of a_j, b_j, and c_j are determined using the sequential quadratic programming method for constrained optimization (Fletcher, 1987). Consequently, the three functions $\rho(s)$, $\theta(s)$, and $\varphi(s)$, or the rod configuration $\mathbf{r}(s)$, are obtained.

3. Numerical results on configurations of confined rod loops with uniform bending stiffness

For a homogeneous rod, D is uniform. In this section, we investigate how the spherical confinement shapes the inextensible thin elastic rod loop of uniform D. We first examine the case that the rod loop is constrained to the spherical surface (i.e., $|\mathbf{r}(s)| = R$) in Section 3.1, and then investigate the case that the rod loop is capable of detaching from the surface (i.e., $|\mathbf{r}(s)| \le R$) in Section 3.2.

3.1. Numerical results on rod configurations and Euler rotation curve approximations

For the homogeneous rod loop confined on the spherical surface of radius R, the radial distance in Eq. (2) is $\rho(s) = R$, and only the coefficients associated with the polar angle function $\theta(s)$ and the azimuthal angle function $\varphi(s)$ are determined via numerical optimization. Selected configurations and corresponding energy profiles of the constrained rod with normalized length $\bar{L} \equiv L/(2\pi R)$ ranging from 1 to 5 are shown in Figs. 2 and 3, respectively. Several sharp configurational transitions are observed between configuration branches in Fig. 2. Each sharp transition corresponds to a critical normalized rod length $\bar{L}_{i\mathrm{cr}}$ (Fig. 3 with $i = 1$ to 9), whose value is numerically determined from the intersection of different energy profiles (represented in different colors in Fig. 3).

Different configuration branches in Fig. 2 are distinguished so that configurational evolution within each branch is continuous, as indicated by the smoothness of each energy profile in Fig. 3, while the transition between different branches is discontinuous, reflected by the energy profile kinks in Fig. 3. By comparing the deformation energy between different branches at the same rod length, stable and metastable states are identified. At a given rod length, the metastable state corresponds to a local energy minimum, whereas the stable state corresponds to a global energy minimum. Each branch comprises both stable and metastable states. Depending on initial configurations of the confined rod loops, both states can be observed in simulations and experiments.

At $\bar{L} \le 1$, the rod loop maintains a planar circular shape with the bending energy $E_{\mathrm{el}} = \pi D/(\bar{L}R)$ (black line in Fig. 3). At the first critical length of $\bar{L}_{1\mathrm{cr}} = 1$, the rod loop coincides with a great circle of the spherical confinement, and beyond $\bar{L}_{1\mathrm{cr}}$ the planar circular loop undergoes out-of-plane buckling into stable saddle-like spatial configurations, oscillating about a great circle (Fig. 2, branch 1 with $\bar{L}_{1\mathrm{cr}} < \bar{L} \le \bar{L}_{2\mathrm{cr}} \approx 1.38$). As the rod length exceeds the second critical length of $\bar{L}_{2\mathrm{cr}}$, stable figure-eight-shaped configurations arise with one self-intersection point (Fig. 2, branch 2 with $\bar{L}_{2\mathrm{cr}} \le \bar{L} \le \bar{L}_{3\mathrm{cr}} = 2$), which has a lower bending energy in comparison with the metastable saddle-shaped configurations in branch 1 in Fig. 2 (Fig. 3). The value of $\bar{L}_{2\mathrm{cr}}$ is determined from the intersection of energy profiles of saddle- and figure-eight-shaped loops. With increasing $\bar{L}$, the upper and lower portions of the figure-eight-shaped loop approach to each other. At the third critical length ($\bar{L}_{3\mathrm{cr}} = 2$), these two portions of the figure-eight-shaped loop collapses together onto a great circle, and the rod loop circumscribes the great circle twice. Once $\bar{L}$ exceeds $\bar{L}_{3\mathrm{cr}}$, the rod buckles into a stable orbitlike configuration with three self-intersection points (Fig. 2, branch 3 with $\bar{L}_{3\mathrm{cr}} < \bar{L} \le \bar{L}_{4\mathrm{cr}} \approx 2.426$), which has a lower bending energy in comparison with the deep saddle-shaped and orbitlike configurations (Fig. 3 and branch 1 in Fig. 2). As $\bar{L}$ exceeds $\bar{L}_{4\mathrm{cr}}$, stable orbitlike configurations arise with four self-intersection points (Fig. 2, branch 1 with $\bar{L}_{4\mathrm{cr}} \le \bar{L} \le \bar{L}_{5\mathrm{cr}} = 3$),

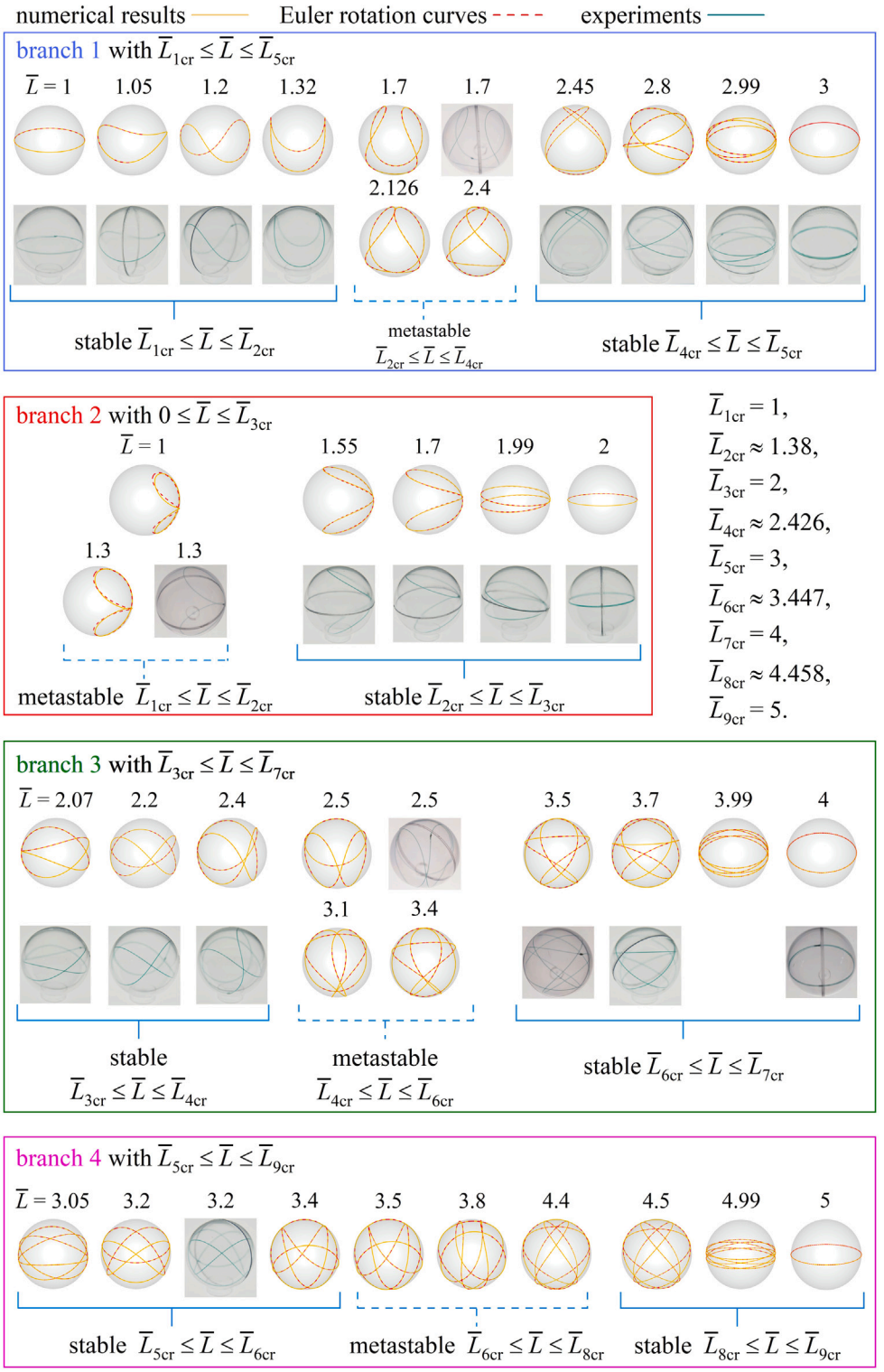

Fig. 2. Selected stable and metastable configurations of a homogeneous rod loop of length L on the spherical confinement of radius R. The normalized rod length is $\bar{L} \equiv L/(2\pi R)$. Experimental results (green profiles, see Note 1 in Supplementary materials for experimental procedures), numerical optimization solutions (yellow solid profiles), and Euler rotation curves (superposed red dashed profiles based on Eq. (4)) are in good agreement. The stable rod configurations have lower energy compared to the metastable configurations of the same rod loop length (see Fig. 3 for energy profiles).

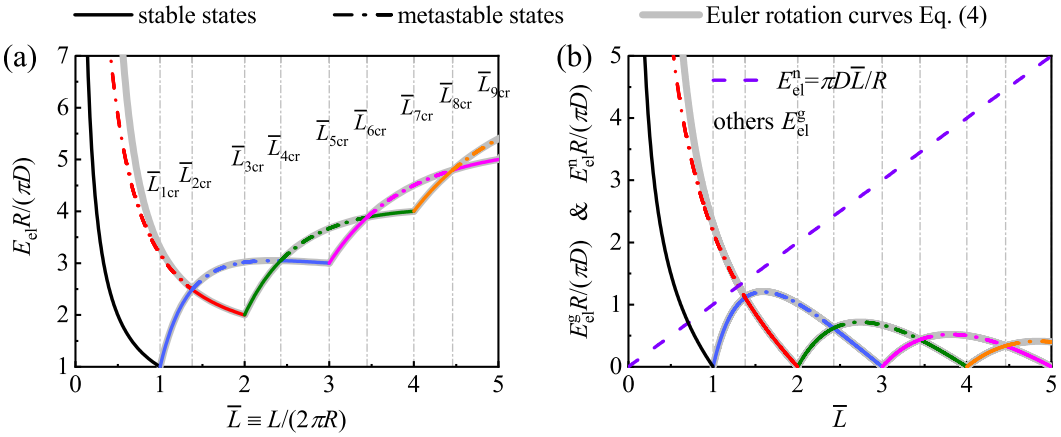

Fig. 3. Numerical results and Euler rotation curve approximations on (a) the normalized elastic energy $E_{el}R/(\pi D)$ and (b) its two components E^n_{el} and E^g_{el} versus the normalized rod length $L/(2\pi R)$. Stable states, thin solid lines; metastable states, dash-dotted lines; Euler rotation curves, thick gray solid lines. Blue, red, green, and pink lines correspond to branches 1 to 4 in Fig. 2, respectively.

which has a lower bending energy in comparison with the metastable orbitlike configurations in branch 2 in Fig. 2 (Fig. 3). The value of $\bar{L}_{4cr}$ is determined from the intersection of energy profiles of saddle-shaped and orbitlike loops. At the fifth critical length of $\bar{L}_{5cr} = 3$, the complex orbitlike configuration collapses onto a great circle, circling it three times. More complex stable and metastable configurations of tangled loops are observed as $\bar{L}$ further increases (Fig. 2), and the corresponding energy profiles are shown in Fig. 3a. It is worth noting that mathematicians have demonstrated that the rods configurations in branch 1 in Fig. 2 are profile curves of 2-lobed constrained Willmore Hopf-tori (Pinkall, 1985; Bohle et al., 2008; Heller, 2014).

The rod loop can achieve a mechanically stable geodesic only when its length is equal to $2m\pi R$ with m as a positive integer ($\bar{L}_{(2m-1)cr} = m$), and the rod loop adopts a circular configuration, encircling a great circle m times. Considering point groups and symmetry, the stable rod configurations at $\bar{L} = m$ are axisymmetric and have $D_{\infty h}$ symmetry with a center of inversion in Schönflies notation (Fig. 2). The stability of the loop configurations on great circles is further analyzed in Section 4.2.

Apart from these axisymmetric configurations, each system configuration in branch 1 demonstrates three perpendicular twofold rotational symmetry axes and two mirror planes, belonging to D_{2d} symmetry. The configurations in branch 2 are with two mirror planes containing a twofold axis and have C_{2v} symmetry. Branch 3 configurations showcase D_{3h} symmetry, and branch 4 configurations exhibit D_{4d} symmetry.

Fig. 2 demonstrates that each rod loop configuration has at least two mirror planes, and the value of η, denoting the η-fold configurational symmetry, appears in the order $\eta = 2, 3, \ldots$ with the increasing branch index (branches 1 and 2 exhibiting twofold symmetry). A closer analysis reveals that the spherically isotropic nature of the spatial confinement and the periodic nature of the rod loops are the foundational physical prerequisites for multiple-fold configurational symmetry. For a surface confinement of an arbitrary shape, no configurational symmetry for the constrained rod loop is expected. The effects of the loop's periodic nature on the constrained rod configuration are more clearly visualized by considering an open thin rod on a sphere. Without the intrinsic smoothness everywhere in closed rod loops, the behavior of surface-constrained open rods is more dependent on boundary conditions. For a constrained open rod with free ends, it stays on a great circle of the spherical confinement, losing length-dependent multiple-fold symmetry. With arbitrarily prescribed end positions and tangent directions, or even free tangent directions at the rod ends, an open rod on a sphere generally loses multiple-fold symmetry (Brunnett and Crouch, 1994).

Introducing the geodesic curvature κ_g and normal curvature κ_n of the surface-constrained rod centerline, one has the relationship $\kappa^2 = \kappa_n^2 + \kappa_g^2$. For the constrained rod loop here as a spherical curve, $\kappa_n^2 = R^{-2}$ (see Appendix A). Then the bending energy E_{el} can be decomposed into two components, the energy E^n_{el} associated with the normal curvature as $E^n_{el} = \int_0^L (D\kappa_n^2/2)\mathrm{d}s = \pi D\bar{L}/R$ and the energy E^g_{el} from the geodesic curvature as $E^g_{el} = \int_0^L (D\kappa_g^2/2)\mathrm{d}s$. The normalized energy $E^n_{el}R/(\pi D)$ is linearly proportional to $\bar{L}$. At large values of $\bar{L}$, the energy contribution from E^n_{el} dominates (Fig. 3b), suggesting that long rod loops tend to adopt configurations consisting of portions slightly deviating from great circles (geodesic). Furthermore, the energy difference in E^g_{el} between different branches diminishes as $\bar{L}$ increases, indicating that the metastable (stable) configurations in branch i and the stable (metastable) configurations in branch $i+1$ become increasingly indistinguishable in energy at extremely large $\bar{L}$.

Similar circle- and saddle-shaped loops predicted in branch 1 in Fig. 2 have also been observed in a wide range of cell activities. In actin-containing vesicles, circular rings of actin bundles linked by muscle filamin can form, and the introduction of Mg^{2+} triggers actin polymerization, resulting in an increase in bundle length and subsequent buckling of the flat ring structures into saddle-shaped loops (Limozin and Sackmann, 2002). Similarly, actin filaments bundled by fascin in stiffened vesicles and protein condensate droplets exhibit similar saddle-shaped configurations (Tsai and Koenderink, 2015). During platelet activation, the marginal band–a peripheral ring structure–buckles from a circle- or oval-shaped loop into a saddle shape, leading to a transition in the spherical cell shape (Diagouraga et al., 2014). The alteration in the morphology of the marginal band loop has been linked to an increase in the

normalized loop length $\bar{L}$, achieved through either an extension of the marginal band length (increasing L) (Diagouraga et al., 2014) or a reduction in cell size (decreasing R) (Dmitrieff et al., 2017). This aligns with the morphological transition from circle to saddle observed in branch 1 (Figs. 2 and 3). Recent theoretical studies indicate that the filament–vesicle system could showcase a variety of morphologies, featuring straight or curved open filaments, as well as crisp, saddle, circle, oval, or twisted saddle-shaped filament loops, depending on the relative stiffness and size of the confined filaments to vesicles (Zou et al., 2018; Shi et al., 2023; Zhang et al., 2024). The evolutionary trajectory from a circular form to a saddle shape and eventually to complex orbit-like configurations with self-intersection has also been observed for loops within evaporating droplets (Sannyamath et al., 2024).

The rod loop configurations in Fig. 2 or the trajectories of the origin of the Frenet–Serret frame, evoke thoughts of the gyroscopic motion which can be described by the Euler rotation. Drawing inspiration from the structure of the rotation matrix for Euler angles, the packing configurations of the confined rod loops in Fig. 2 are well described by the Euler rotation curve approximation, defined by the following parametric equations

$$\begin{aligned} x(t) &= R[-\cos\alpha\cos t\cos(lt)+\sin t\sin(lt)],\\ y(t) &= R[\cos\alpha\sin t\cos(lt)+\cos t\sin(lt)], \qquad \alpha\in[0,\pi], t\in[0,2\pi],\\ z(t) &= R\sin\alpha\cos(lt), \end{aligned} \tag{4}$$

where the parameter l is a positive integer governing the periodicity of the rod configuration. Eq. (4) can be geometrically interpreted as the path traced by the origin of the Frenet–Serret frame during uniform motion along a particular great circle of a rotating sphere. Parameterization variants of the tangent vector $\mathbf{t}$ could also give combinations of the trigonometric functions in Eq. (4). The prescribed rod length L is given as

$$L = R\frac{l+\cos\alpha}{l}\mathrm{E}\left(2l\pi, \frac{\sqrt{-1}\sin\alpha}{l+\cos\alpha}\right), \tag{5}$$

where $\mathrm{E}(\phi,K)=\int_0^{\phi}\sqrt{1-K^2\sin^2\nu}\mathrm{d}\nu$ denotes the incomplete elliptic integral of the second kind, and $\bar{L}\in[(l-1),(l+1)]$. In the limiting case of $l\to\infty$, $\lim_{l\to\infty}\bar{L}=l+\cos\alpha$ and $\lim_{l\to\infty}E_{\mathrm{el}}^{\mathrm{g}}/E_{\mathrm{el}}^{\mathrm{n}}=0$. Fig. 4 shows the $\bar{L}$–α relationship at given l.

With the analytical expression in Eq. (4), the curvature κ and torsion τ of the rod configuration approximated by the Euler rotation curve are respectively obtained as

$$\kappa=\frac{|\mathbf{r}_{,t}\times\mathbf{r}_{,tt}|}{|\mathbf{r}_{,t}|^3} \quad\text{and}\quad \tau=\frac{\mathbf{r}_{,t}\cdot(\mathbf{r}_{,tt}\times\mathbf{r}_{,ttt})}{|\mathbf{r}_{,t}\times\mathbf{r}_{,tt}|^2}. \tag{6}$$

Substituting κ in Eq. (6) into Eq. (2), the elastic energy of the rod can be obtained.

While the Euler rotation curve in Eq. (4) is not an exact solution to the problem of minimizing the total squared curvature of a closed spherical curve, it offers a simple analytical expression of the rod configuration, proving valuable for quick estimations and calculations, and demonstrating strong predictive capabilities (Figs. 2 and 3). Comparison of additional rod configurations between numerical results and the Euler rotation curve approximations can be found in Figs. S2–S5 in Supplementary materials.

At $l=1$, Eq. (4) reduces to the parameterization of a hippopede, a figure-eight-shaped curve of intersection between the spherical confinement and a tangent circular cylinder of radius $R\sin^2(\alpha/2)$. At $l=1$ and $\alpha=\pi/4$, the figure-eight-shaped curve reduces to the Viviani curve. The hippopede approximates the (meta)stable equilibrium configuration of the elastic rod loop constrained to a spherical surface very well in the range of $\bar{L}\in[1,2]$ (Fig. 2 and the gray line covering the red line in Fig. 3).

At $l=2$, by introducing $a=R(1-\cos\alpha)/2$ and $b=R(1+\cos\alpha)/2$, the Euler rotation curve describe by Eq. (4) turns into the seam line curve of a tennis ball with radius $R=a+b$, which can be expressed equivalently as (Rogers and Adams, 1990)

$$x=a\cos t-b\cos(3t),\quad y=a\sin t+b\sin(3t),\quad z=2\sqrt{ab}\cos(2t),\qquad t\in[0,2\pi]. \tag{7}$$

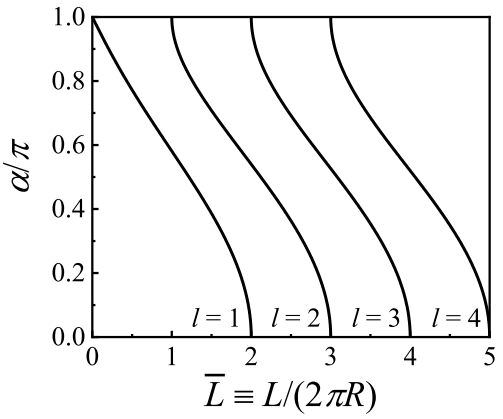

Fig. 4. The $\bar{L}$–α relationship at given l given by Eq. (5). Here, $l=1$, 2, 3, and 4 correspond to configurations in branches 2, 1, 3, and 4 in Fig. 2, respectively.

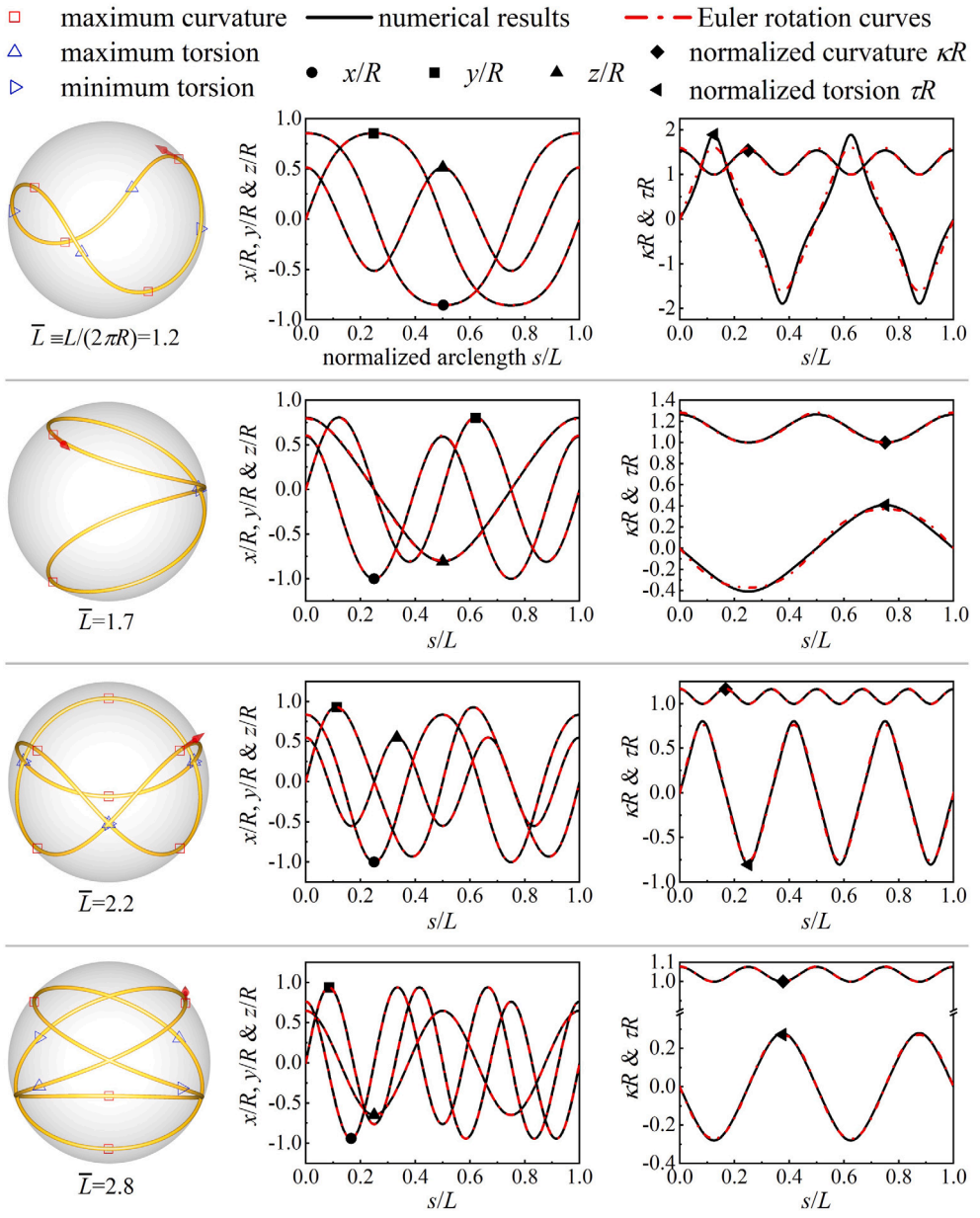

Fig. 5. Numerical optimization results and Euler rotation curve approximations on the configuration coordinates x/R, y/R, z/R, normalized curvature κR, and normalized torsion τR of the surface-constrained rod loops with $\bar{L} \equiv L/(2\pi R) = 1.2$ (branch 1), 1.7 (branch 2), 2.2 (branch 3), and 2.8 (branch 1). To ensure alignment, possible rigid body rotations and mirror symmetry are applied to the Euler rotation curve approximations and numerical results to match them together. Here the reference point of $s = 0$ is chosen such that the curvature of the constrained rod, $\kappa(s = 0)$, attains its maximum value. Numerical results (solid profiles) and Euler rotation curves (superposed red dash-dotted profiles) are in good agreement. Red arrows in numerical configurations denote $\mathbf{t}(s = 0)$.

The prescribed rod length L based on Eq. (7) is

$$L = 4(3R - 2a)\mathrm{E}\left(\frac{\pi}{2}, \frac{2\sqrt{a(a-R)}}{3R-2a}\right). \tag{8}$$

The tennis-ball seam line closely approximates the (meta)stable equilibrium configuration of the confined rod loop on the sphere, with the total length ranging from one to three times that of the great circle ($\bar{L} \in [1, 3]$, Fig. 2 and the gray line covering the blue line in Fig. 3). For a rod loop constrained to an elastic spherical confinement, the rod loop configuration deviates from the tennis-ball curve, since both the elastic loop and confinement deform. In the case of packing flexible filaments in vesicles, additional terms such as $\cos(2t)$ in x and $\cos t$ in z are introduced to characterize the crisp- and saddle-shaped filament loops (Shi et al., 2023).

Further examinations of higher-order geometric properties, curvature κ and torsion τ, of the rod configurations based on the Euler rotation curve approximations (Eqs. (4) and (6)) are depicted in Fig. 5, showing good agreement with numerical results. The torsion profiles in Fig. 5 further validate classical theorems in differential geometry, including that total torsion of a closed spherical curve vanishes ($\oint \tau(s)\mathrm{d}s = 0$) (Geppert, 1941; Millman and Parker, 1977) and that the torsion of a simple closed convex space curve in the three-dimensional Euclidean space $\mathbb{R}^3$ must change sign at least four times (Thorbergsson and Umehara, 1999; Ghomi, 2019).

3.2. Homogeneous rod loops enclosed within the spherical confinement

In Section 3.1, the rod loop is constrained to the inner surface of the spherical confinement. If the homogeneous rod is enclosed within the spherical confinement but not constrained to the surface–meaning the radial motion of the rod is unrestricted toward the sphere center–it is interesting to observe that identical stable rod configurations to those in Section 3.1 can be achieved (for $1 \le \bar{L} \le 3$ we have numerically checked). It is hypothesized that enclosed homogeneous rod loops of $\bar{L} \ge 1$ remain fully attached to the spherical surface without any detachment. Therefore, the analysis in the following section on homogeneous loops is concentrated on the spherical surface-constrained loops, with the conclusions applicable to rod loops confined within the spherical enclosures.

A related yet distinct phenomenon involves two-dimensional packing of elastic rings within rigid or elastic confinement. In this scenario, out-of-plane deformation is prohibited, necessitating the folding of long confined rings away from the confinement. This folding can result in the formation of multiple discrete or continuous self-contact regions, as well as regions of contact with the confinement. Both symmetric and asymmetric equilibrium configurations are observed (Boué et al., 2006; Lombardo et al., 2018).

4. Analytical solutions for configuration and force properties of surface-constrained rod loops

To gain a deep, clear and insightful understanding of mechanical principles governing the packing behavior of surface-constrained rod loops, analytical solutions and asymptotic analysis are sought. Based on the local equilibrium of force and moment, we adopt a theoretical framework proposed for elastic rods constrained to general surfaces to model rod loop deformation (Wang and Yi, 2024). This approach allows us to determine the internal and contact forces experienced by the rods, which cannot be obtained from the numerical optimization method described in Section 2. Compared to general confining surfaces, the inherent high degree of symmetry of the spherical confinement simplifies geometric problems, enabling the analytical determination of the forces and equilibrium configurations of the enclosed rod loops. Our analysis shows that the internal and contact forces experienced by the rod loops constrained to spherical surfaces can be characterized by the geodesic curvature, which further leads to analytical results, including stability analysis and solutions for the configurations and experienced forces of the rod loops.

4.1. Theoretical framework with consideration of rod inhomogeneity

Equilibrium equations articulating the balance of forces and moments for the inhomogeneous rod of $D(s)$, respectively, are (Landau and Lifshitz, 1986; Audoly and Pomeau, 2010)

$$\mathbf{F}' + \mathbf{q} = \mathbf{0}, \tag{9}$$

$$\mathbf{M}' + \mathbf{r}' \times \mathbf{F} = \mathbf{0}, \tag{10}$$

where $\mathbf{F}(s)$ and $\mathbf{M}(s)$ are the internal force and internal moment, respectively, acting on the cross-section at arclength s, and $\mathbf{q}(s)$ denotes the line load on the rod (e.g., here the contact force per unit length due to the spherical confinement). For the rod devoid of torsional strain energy, $\mathbf{M}$ acting as the bending moment is given by (Landau and Lifshitz, 1986; Audoly and Pomeau, 2010)

$$\mathbf{M} = D\kappa\mathbf{b}, \tag{11}$$

where $\mathbf{b}(s)$ is the unit binormal vector of the rod centerline curve and obeys $\mathbf{b} = \mathbf{t} \times \mathbf{n}$ with the unit tangent vector $\mathbf{t} = \mathbf{r}'$ and unit principal normal vector $\mathbf{n} = \mathbf{t}'/|\mathbf{t}'| = \mathbf{t}'/\kappa$. The contact force, normal to the spherical surface, is expressed as

$$\mathbf{q} = -\lambda \mathbf{e}_r, \tag{12}$$

where $\mathbf{e}_r$ is the outward-pointing unit normal vector of the spherical surface (Appendix A).

Substituting Eqs. (11) and (12) into Eqs. (9) and (10) gives

$$\mathbf{F}' - \lambda \mathbf{e}_r = \mathbf{0} \quad \text{and} \quad (D'\kappa + D\kappa')\mathbf{b} - D\kappa\tau\mathbf{n} + \mathbf{t} \times \mathbf{F} = \mathbf{0}, \tag{13}$$

where $\mathbf{b}' = -\tau\mathbf{n}$ has been used, and the torsion of the rod centerline is $\tau = -\mathbf{n} \cdot \mathbf{b}' = \mathbf{r}' \cdot (\mathbf{r}'' \times \mathbf{r}''')/|\mathbf{r}''|^2$.

Projecting Eq. (13) onto the basis vectors $\mathbf{t}$, $\mathbf{n}$, and $\mathbf{b}$ of the Frenet–Serret frame $\{\mathbf{t}, \mathbf{n}, \mathbf{b}\}$ and introducing componential forms $\mathbf{F} = F_\mathrm{t}\mathbf{t} + F_\mathrm{n}\mathbf{n} + F_\mathrm{b}\mathbf{b}$, one has five independent equations (Wang and Yi, 2024)

$$F_\mathrm{t}' - \kappa F_\mathrm{n} = 0, \tag{14}$$

$$F_\mathrm{n}' + \kappa F_\mathrm{t} - \tau F_\mathrm{b} - \lambda\kappa_\mathrm{n}/\kappa = 0, \tag{15}$$

$$F_\mathrm{b}' + \tau F_\mathrm{n} - \lambda\kappa_\mathrm{g}/\kappa = 0, \tag{16}$$

$$F_\mathrm{b} = -D\kappa\tau, \tag{17}$$

$$F_\mathrm{n} = -D'\kappa - D\kappa', \tag{18}$$

where relations $\mathbf{e}_r \cdot \mathbf{n} = \kappa_n/\kappa$ and $\mathbf{e}_r \cdot \mathbf{b} = \kappa_g/\kappa$ have been used, with κ_g as the geodesic curvature and κ_n as the normal curvature of the rod centerline (see Appendix A). The moment balance along $\mathbf{t}$ holds spontaneously. For a spherical curve, $\kappa_n = -1/R$. Then F_t and λ can be solved in terms of geometric parameters κ and τ from Eqs. (14)–(18).

For a rod loop staying on the great circle of the spherical confinement, one has $\kappa_g = 0$, $\kappa = -\kappa_n = 1/R$, and $\tau = 0$. In this case, Eqs. (15), (17), and (18) reduce to

$$F_t = D'' - \lambda R, \qquad F_b = 0, \quad \text{and} \quad F_n = -D'/R. \tag{19}$$

Eq. (16) holds spontaneously. Substituting Eq. (19) into Eq. (14) gives a governing equation for λ, $D'/R^2 + D''' = \lambda' R$, solved as

$$\lambda = C + \int_0^s \left(\frac{D'}{R^3} + \frac{D'''}{R} \right) \mathrm{d}s, \tag{20}$$

where C is a constant of integration. For the case of uniform bending stiffness, one has a uniform contact force $\lambda = C$ for the rod loop staying on the great circle.

In the following analysis, we focus on the case of $\kappa_g \neq 0$. From Eqs. (15)–(18), λ and F_t are solved as

$$\lambda = -\frac{\kappa}{\kappa_g}(2D'\kappa\tau + 2D\kappa'\tau + D\kappa\tau'), \tag{21}$$

$$F_t = D'' + 2D'\frac{\kappa'}{\kappa} + D\frac{\kappa''}{\kappa} - D\tau^2 + \frac{2D'\kappa\tau + 2D\kappa'\tau + D\kappa\tau'}{\kappa_g \kappa R}. \tag{22}$$

For the rod centerline on the spherical surface (a spherical curve), one has

$$\kappa_g = \kappa\cos\omega, \qquad \kappa_n = -\kappa\sin\omega = -1/R, \qquad \tau_g = 0, \quad \text{and} \quad \tau = \tau_g - \omega' = -\omega', \tag{23}$$

where τ_g is the geodesic torsion of the rod centerline, and ω is the angle between the unit binormal vector $\mathbf{b}$ and the unit normal vector $\mathbf{e}_r$ to the confining surface (Appendix A). In Appendix A, for a curve on a surface, the unit normal vector $\mathbf{n}_S$ to the confining surface is introduced in the context of the Darboux frame. For the spherical surface considered in this work, $\mathbf{e}_r = \mathbf{n}_S$.

Then these three internal force components F_b, F_n, and F_t given by Eqs. (17), (18), and (22), respectively, together with contact force λ in Eq. (21), are expressed as functions of κ_g with the help of Eqs. (A.1)–(A.3) as

$$F_b = -\frac{D\kappa_g'}{\sqrt{1 + R^2\kappa_g^2}}, \tag{24}$$

$$F_n = -D'\frac{\sqrt{1 + R^2\kappa_g^2}}{R} - D\frac{R\kappa_g\kappa_g'}{\sqrt{1 + R^2\kappa_g^2}}, \tag{25}$$

$$F_t = D'' + 2D'\frac{\kappa_g'}{\kappa_g} + D\frac{\kappa_g''}{\kappa_g} = \frac{(D\kappa_g)''}{\kappa_g}, \tag{26}$$

$$\lambda = -\frac{2D'\kappa_g' + D\kappa_g''}{\kappa_g R}. \tag{27}$$

Substituting Eqs. (25) and (26) into Eq. (14) gives a governing differential equation for κ_g as

$$D''' + D'\left(\frac{1}{R^2} + \frac{\kappa_g^4 - 2\kappa_g'^2 + 3\kappa_g\kappa_g''}{\kappa_g^2} \right) + \frac{\kappa_g'[2D''\kappa_g + D(\kappa_g^3 - \kappa_g'')] + D\kappa_g\kappa_g'''}{\kappa_g^2} = 0. \tag{28}$$

4.2. Stability and force analysis for homogeneous rod loops on great circles

As suggested by Eq. (20), the contact force applied by the spherical confinement onto the constrained loop staying on the great circle is uniform, but its value is not determined. In comparison with classical results on the buckling load of unconstrained circular rings under different types of loading pressure (Timoshenko and Gere, 1961; Singer and Babcock, 1970), there remains a notable absence of formulated analysis or clarity regarding the buckling behavior of surface-constrained loops, even when subjected to spherical confinement. In this section, we focus on the buckling and force analysis for homogeneous rod loops staying on great circles.

Substituting Eqs. (17) and (18) into Eq. (16) and taking $D' = 0$ give

$$D\kappa(\kappa\tau)' + D\kappa\kappa'\tau + \lambda\kappa_g = 0. \tag{29}$$

With the aid of Eqs. (A.2) and (A.3), along with the relationships $\kappa_n = -1/R$ and $\tau_g = 0$, Eq. (29) simplifies to

$$\kappa_g'' + \frac{\lambda R}{D}\kappa_g = 0 \quad \text{or} \quad \kappa_g'' + \beta^2\kappa_g = 0, \tag{30}$$

with the notation $\beta^2 = \lambda R/D$ under the assumption of a positive value of λ (indicating an inward-pointing compressive contact force). The solution to Eq. (30) is

$$\kappa_g = A\cos(\beta s) + B\sin(\beta s), \tag{31}$$

where A and B denote constants determined through boundary conditions.

For a buckled loop just deviating slightly from a great circle of vanishing geodesic curvature, there are certain points where $\kappa_g = 0$ still holds. To simplify the analysis in this section, one of these points with vanishing geodesic curvature is selected as $s = 0$.

The continuity condition $\kappa_g(s = 0) = \kappa_g(s = L) = 0$ necessitates $A = 0$ and $\sin(\beta L) = 0$, and then the smoothness condition $\kappa_g'(s = 0) = \kappa_g'(s = L)$ leads to $\cos(\beta L) = 1$. Combining these conditions yields $A = 0$ and $\beta L = 2n\pi$ with positive integer $n = 1, 2, 3, \ldots$, and

$$\kappa_g = B \sin \frac{2n\pi s}{L}. \tag{32}$$

Here trivial cases of circular configurations without out-of-plane deformation ($\kappa_g(s) = 0$ with $A = B = 0$ or $A = \beta = 0$) are excluded.

The analysis above indicates that for the rod loop with a length of $L = 2m\pi R$ (m as a positive integer) and adopting an m-tuple cover of a great circle, the relation $n = m, m \pm 1, \ldots$ is required. A careful examination of the profile of $\kappa_g(s)$ in Eq. (32) suggests that $n = m$ corresponds to the buckled rod loop crossing the sphere equator (a specified geodesic circle) $2m$ times, with each rod portion covering the great circle undergoing rotation about a shared axis passing through the sphere center and the great circle. Such deformation with biased rotation disrupts the system symmetrical properties stemming from the spherical confinement, and renders the rod configuration inherently unstable. Consequently, $n = m$ corresponds to unstable buckled configurations.

Then $n = m \pm 1$ is adopted, as the nearest integer of m, for stable buckled loops of m-tuple covers of a great circle ($L = 2m\pi R$) with $\beta = 2(m \pm 1)\pi/L$. At $n = m + 1$, the buckled loops oscillate about the great circle with $\kappa_g = B \sin[(m + 1)s/(mR)]$, and gradually deviate from the great circle as the rod length increases. The corresponding critical load λ_{cr} is given as

$$\lambda_{cr} = \frac{D\beta^2}{R} = \frac{D}{R^3}\frac{(m+1)^2}{m^2} \quad (m = 1, 2, 3, \ldots). \tag{33}$$

At $n = m - 1$, the buckled loops oscillate about the great circle with $\kappa_g = B \sin[(m - 1)s/(mR)]$, and gradually collapse onto the great circle as the rod length increases. The corresponding critical load λ_{cr} is

$$\lambda_{cr} = \frac{D\beta^2}{R} = \frac{D}{R^3}\frac{(m-1)^2}{m^2} \quad (m = 2, 3, 4, \ldots). \tag{34}$$

Both Eqs. (33) and (34) indicate that $\lambda_{cr} \to D/R^3$ as $m \to \infty$. Using perturbative analysis with approximation of $\kappa_g \sim \cos(n\varphi/m)$ or $\kappa_g \sim \cos[(m + 1)\varphi/(m + 2)]$, the results in Eqs. (33) and (34) have been obtained (Guven and Vázquez-Montejo, 2012).

4.3. Formulated analysis on force and configurations of constrained homogeneous rod loops

We now seek theoretical derivations on force and configurations of constrained homogeneous rod loops. Eq. (28) of κ_g for the inhomogeneous rod loops is too complex to be solved analytically. Fortunately, an analytical solution of κ_g is found for homogeneous rod loops. For the homogeneous rod ($D' = 0$), Eq. (28) reduces to

$$\kappa_g \kappa_g''' + \kappa_g'(\kappa_g^3 - \kappa_g'') = 0,$$

and a solution is (Langer and Singer, 1984; Guven and Vázquez-Montejo, 2012)

$$\kappa_g = \pm 2ck\,\mathrm{cn}(cs, k), \tag{35}$$

where parameters c and k can be determined by closure conditions of the rod loop, and $\mathrm{sn}(cs, k)$, $\mathrm{cn}(cs, k)$, and $\mathrm{dn}(cs, k)$ are three most popular Jacobi elliptic functions defined via the inverse of the incomplete elliptic integral of the first kind as $\mathrm{sn}(u, k) = \sin(\mathrm{am}(u, k))$, $\mathrm{cn}(u, k) = \cos(\mathrm{am}(u, k))$, and $\mathrm{dn}(u, k) = \sqrt{1 - k^2\mathrm{sn}^2(u, k)}$ with the Jacobi amplitude $\mathrm{am}(u, k)$ satisfying $u = \int_0^{\mathrm{am}(u,k)}(1 - k^2 \sin^2\theta)^{-1/2}\mathrm{d}\theta$. The dimension of c is reciprocal length and k is dimensionless. The positive and negative signs in Eq. (35) signify two equivalent solutions, each corresponding to rod loop configurations that are mirror images of each other. Hereinafter $\kappa_g = -2ck\,\mathrm{cn}(cs, k)$ is taken for further discussion. Then the curvature κ and torsion τ of the rod centerline are obtained, respectively, as

$$\kappa = \sqrt{\kappa_n^2 + \kappa_g^2} = \frac{1}{R}\sqrt{1 + 4c^2k^2R^2\mathrm{cn}^2(cs, k)} \quad \text{and} \quad \tau = \frac{2c^2kR\,\mathrm{dn}(cs, k)\mathrm{sn}(cs, k)}{1 + 4c^2k^2R^2\mathrm{cn}^2(cs, k)}. \tag{36}$$

At $D' = 0$, the internal force components are expressed as

$$F_t = c^2D[1 - 2\mathrm{dn}^2(cs, k)], \quad F_n = \frac{4c^3Dk^2R\,\mathrm{cn}(cs, k)\mathrm{dn}(cs, k)\mathrm{sn}(cs, k)}{\sqrt{1 + 4c^2k^2R^2\mathrm{cn}^2(cs, k)}}, \quad \text{and} \quad F_b = -\frac{2c^2Dk\,\mathrm{dn}(cs, k)\mathrm{sn}(cs, k)}{\sqrt{1 + 4c^2k^2R^2\mathrm{cn}^2(cs, k)}}, \tag{37}$$

and the contact force λ is

$$\lambda = \frac{c^2D}{R}[2\mathrm{dn}^2(cs, k) - 1]. \tag{38}$$

Eq. (38) can also be obtained using the calculus of variations (Guven and Vázquez-Montejo, 2012).

So far parameters c and k in Eq. (35) are unknown and yet to be determined using closure conditions of angles θ and φ as follows.

As $\mathbf{r}$ is parallel to the contact force $\mathbf{q}$, one has $\mathbf{r} \times \mathbf{F}' = \mathbf{0}$ based on Eq. (9). Combining $\mathbf{r} \times \mathbf{F}' = \mathbf{0}$ and Eq. (10), the relation $\mathbf{M}' + (\mathbf{r} \times \mathbf{F})' = \mathbf{0}$ holds, which means that the vector $\mathcal{M} = \mathbf{M} + \mathbf{r} \times \mathbf{F}$ is conserved along the arclength s. Here $\mathcal{M}$ can be interpreted as the resultant moment per unit length about the sphere center. Aligning $\mathcal{M}$ along a given direction enables the specification of the orientation of the confined rod loops.

In the Darboux frame $\{\mathbf{r};\mathbf{t},\mathbf{g},\mathbf{n}_S\}$ of the rod curve (Appendix A), $\mathbf{n}_S(=\mathbf{e}_r)$ is the unit normal vector to the confining surface and $\mathbf{g}$ is the unit tangent normal vector or conormal vector with $\mathbf{g}=\mathbf{n}_S\times\mathbf{t}$. Then $\mathbf{M}=D\kappa\mathbf{b}$ can be rewritten by projecting $\kappa\mathbf{b}$ onto the $\{\mathbf{t},\mathbf{g},\mathbf{n}_S\}$ basis as

$$\mathbf{M}=D\kappa_g\mathbf{n}_S-D\kappa_n\mathbf{g}. \tag{39}$$

Using $\mathbf{F}=F_t\mathbf{t}+F_{n_S}\mathbf{n}_S+F_g\mathbf{g}$, $\mathbf{r}=R\mathbf{n}_S$, and Eq. (39), $\boldsymbol{\mathcal{M}}$ is expressed as

$$\boldsymbol{\mathcal{M}}=-F_gR\mathbf{t}+D\kappa_g\mathbf{n}_S-(D\kappa_n-F_tR)\mathbf{g}, \tag{40}$$

where $F_t=D\kappa_g''/\kappa_g$ from Eq. (26) and $F_g=\mathbf{F}\cdot\mathbf{g}=(F_n\kappa_g-F_g\kappa_n)/\kappa$. The relation $F_{n_S}=\mathbf{F}\cdot\mathbf{n}_S=(F_n\kappa_n+F_b\kappa_g)/\kappa=0$ has also been used. Combining Eqs. (24)–(26), $\boldsymbol{\mathcal{M}}$ in Eq. (40) can be expressed as a function of κ_g

$$\boldsymbol{\mathcal{M}}=DR\kappa_g'\mathbf{t}+D\kappa_g\mathbf{n}_S+D\left(\frac{1}{R}+\frac{R\kappa_g''}{\kappa_g}\right)\mathbf{g}. \tag{41}$$

Substituting Eq. (35) into Eq. (41), the magnitude of $\boldsymbol{\mathcal{M}}$ is obtained as

$$\mathcal{M}=\frac{D}{R}\sqrt{(c^2R^2-1)^2+4k^2c^2R^2}. \tag{42}$$

As the system can always be rotated such that $\boldsymbol{\mathcal{M}}$ aligns along z-axis, $\boldsymbol{\mathcal{M}}=-\mathcal{M}\mathbf{e}_z$ is taken (Guven and Vázquez-Montejo, 2012). Then one has

$$\boldsymbol{\mathcal{M}}\cdot\mathbf{n}_S=-\mathcal{M}\mathbf{e}_z\cdot\mathbf{e}_r=-\mathcal{M}\cos\theta, \tag{43}$$

$$\boldsymbol{\mathcal{M}}\cdot\mathbf{g}=-\mathcal{M}\mathbf{e}_z\cdot\mathbf{g}=-\mathcal{M}R\varphi'\sin^2\theta. \tag{44}$$

Combining Eqs. (35), (42), and (43) with $\boldsymbol{\mathcal{M}}\cdot\mathbf{n}_S=D\kappa_g$ from Eq. (41), one can obtain

$$\cos\theta=\frac{2cRk\,\mathrm{cn}(cs,k)}{\sqrt{(c^2R^2-1)^2+4k^2c^2R^2}}. \tag{45}$$

Combining Eq. (44) with $\boldsymbol{\mathcal{M}}\cdot\mathbf{g}=D(\kappa_g+R^2\kappa_g'')/(R\kappa_g)$ from Eq. (41), one has

$$-\mathcal{M}R\varphi'\sin^2\theta=\frac{D(\kappa_g+R^2\kappa_g'')}{R\kappa_g}. \tag{46}$$

Substituting Eqs. (35) and (45) into Eq. (46), the azimuthal angle φ obeys

$$\varphi'=\frac{D\mathcal{M}}{R^2}\times\frac{1+c^2R^2-2c^2R^2\mathrm{dn}^2(cs,k)}{\mathcal{M}^2-4c^2D^2k^2\mathrm{cn}^2(cs,k)}. \tag{47}$$

Integrating Eq. (47) with $\varphi(0)=0$, the azimuthal angle $\varphi(s)$ can be expressed as

$$\varphi(s)=-\frac{\sqrt{(c^2R^2-1)^2+4k^2c^2R^2}}{2cR}\left[cs-\frac{c^2R^2+1}{c^2R^2-1}\Pi\left(-\frac{4k^2c^2R^2}{(c^2R^2-1)^2};\mathrm{am}(cs,k),k\right)\right], \tag{48}$$

where $\Pi(\nu;\phi,k)=\int_0^\phi(1-\nu\sin^2\varsigma)^{-1}(1-k^2\sin^2\varsigma)^{-1/2}\mathrm{d}\varsigma$ is the incomplete elliptic integral of the third kind. The rod configuration can be characterized by $\theta(s)$ and $\varphi(s)$ given by Eqs. (45) and (48), which indicate independence of the homogeneous bending stiffness D.

Values of c and k in Eqs. (45) and (48) are determined using closure conditions of the rod loop. With $\cos\theta\sim\mathrm{cn}(cs,k)$ seen from Eq. (45) and the periodicity relation $\mathrm{cn}(u,k)=-\mathrm{cn}[u+2\mathrm{K}(k),k]$, the periodicity of the polar angle function $\theta(s)$ requires

$$c=\eta\frac{4\mathrm{K}(k)}{L}, \tag{49}$$

where η is a positive integer denoting the number of complete periods of $\theta(s)$ (e.g., $\eta=1$ for rod configurations in branch 2, $\eta=2$ for branch 1; $\eta=3$ for branch 3; $\eta=4$ for branch 4) and $\mathrm{K}(k)=\int_0^{\pi/2}(1-k^2\sin^2\theta)^{-1/2}\mathrm{d}\theta$ is the complete elliptic integral of the first kind. Taking $\varphi(0)=0$, the periodicity of the azimuthal angle function $\varphi(s)$ requires

$$\varphi(L)=\varphi(0)+2\pi p=2\pi p, \tag{50}$$

where p is a positive (negative) integer representing the count of times the rod loop encircles z-axis in the positive (negative) azimuthal direction (e.g., $p=-2$ for rod configurations at $\bar{L}=1.55$, 1.7, and 1.99 in branch 2; $p=-3$ for $\bar{L}=2.45$, 2.8, and 2.99 in branch 1; $p=-4$ for $\bar{L}=3.5$, 3.7, and 3.99 in branch 3). At $p=0$, metastable figure-eight-shaped configurations in branch 2 in Fig. 2 are observed (e.g., $\bar{L}=1$ and 1.3 in branch 2).

In general, values of parameters c and k can be numerically obtained from Eqs. (49) and (50) at a given rod length L. In cases where the constrained rod has a slight deviation away from the great circle, k^2 is small (Fig. 11 in Appendix B) and its analytical approximation could be obtained (Eq. (B.4) in Appendix B). It is shown that geometric quantities κ and τ, as well as the contact force λ, can all be well approximated by employing Eq. (B.4) (Fig. 11 in Appendix B).

The analytical solution derived from the local force and moment balance equations in Section 4.3 leads to results akin to those obtained through the previous variational framework (Guven and Vázquez-Montejo, 2012). However, a notable distinction lies in the

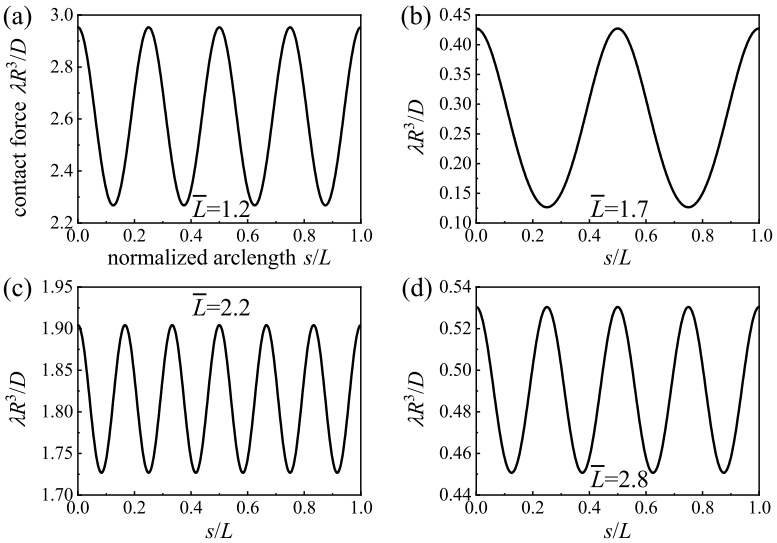

Fig. 6. The normalized contact force $\lambda R^3/D$ versus the normalized arclength s/L at $\bar{L} \equiv L/(2\pi R) = 1.2$, 1.7, 2.2, and 2.8. Analytical findings (Eqs. (38), (49), and (50)) and numerical optimization solutions yield identical results. Values of (n, p) sets from (a) to (d) are $(2, 1)$, $(1, -2)$, $(3, 2)$, and $(2, -3)$, respectively.

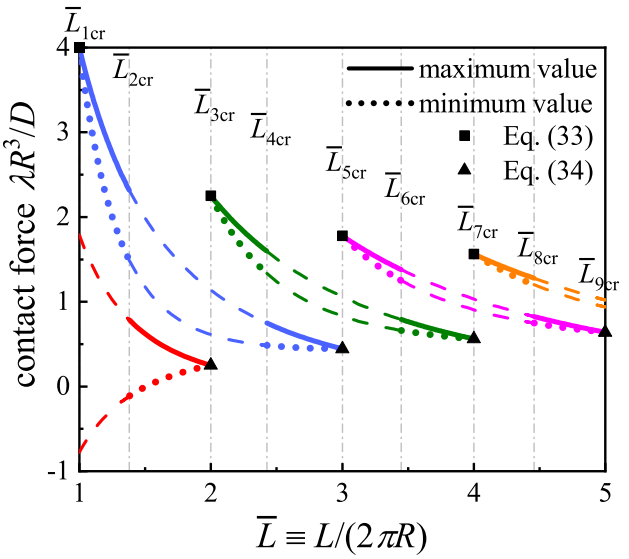

Fig. 7. Maximum and minimum values of the normalized contact force $\lambda R^3/D$ for stable solutions (thick solid and dotted lines) and metastable solutions (thin dashed lines). Color lines correspond to cases in Fig. 3. Analytical findings and numerical optimization solutions yield identical results. Solid square and triangle symbols denote results from Eqs. (33) and (34), respectively.

absence of introducing any constant of integration in the current analysis. This deviation arises from circumventing the integration of the tangential force balance equation.

Eq. (27) indicates that the contact force magnitude λ is determined by local geometric and material properties. For the homogeneous rod loop, $\lambda = -(D\kappa_g'')/(R\kappa_g)$. Using Eqs. (38), (49), and (50) or via numerical optimization, the contact force distributions for the stable configurations in Fig. 5 of different loop lengths are evaluated in Fig. 6. The configurations in cases (a) and (d) have D_{2d} symmetry, while the configuration in case (b) displays C_{2v} symmetry, and that in case (c) exhibits T_d symmetry. The progression of configurational symmetry from D_{2d} to C_{2v} and then to T_d is reflected in periods of λ profiles, transitioning from $s/(4L)$ to $s/(2L)$ and then to $s/(6L)$.

By extracting the maximum and minimum values of the normalized contact force $\lambda R^3/D$ at various $\bar{L}$ values, the upper and lower bounds of the contact force are obtained (Fig. 7). Extreme values of λ show features of nonmonotonicity and discontinuity due to the configurational transitions with increasing $\bar{L}$. With the exception of the minimum values of λ at $\bar{L}$ around 1.5, which are negative, all other minimum values and all maximum values of λ are positive. This indicates that, in most instances, the contact

force exerted by the spherical surface onto the rods tends to push the loops inward radially, impeding the loop expansion. In a few instances of branch 2, the contact force brings partial regions of the confined loops to attach to the inner surface.

The critical contact force presented in Fig. 7 agree with Eqs. (33) and (34). At $\bar{L}$ approaches 1, the normalized contact force applied on the circular loop tends to $\lambda_{1\mathrm{cr}}R^3/D = 4$. In contrast, the critical external pressure P_{ext} for an elastic ring of length $2\pi R$ undergoing planar buckling conforms to distinct relations: $P_{\mathrm{ext}}^{\mathrm{I}}R^3/D = 3$ under hydrostatic pressure (case I) (Boresi, 1955; Timoshenko and Gere, 1961), $P_{\mathrm{ext}}^{\mathrm{II}}R^3/D \approx 3.27$ under constant directional pressure (case II) (Chwalla and Kollbrunner, 1938; Singer and Babcock, 1970), and $P_{\mathrm{ext}}^{\mathrm{III}}R^3/D = 4.5$ under centrally directed pressure (case III) (Boresi, 1955). The anticipation of $\lambda_{1\mathrm{cr}} > P_{\mathrm{ext}}^{\mathrm{I}}$ and $\lambda_{1\mathrm{cr}} > P_{\mathrm{ext}}^{\mathrm{II}}$ arises due to the exclusion of planar deformation of the spherical surface-constrained loop, whereas the expectation of $\lambda_{1\mathrm{cr}} < P_{\mathrm{ext}}^{\mathrm{III}}$ stems from the availability of out-of-plane deformation of the spherical loop.

5. Effects of bending stiffness inhomogeneity on packing of surface-constrained rod loops

The surface-constrained inhomogeneous rod loop comprises a softer segment and a stiffer segment. A hyperbolic tangent function is employed to specify the inhomogeneity of the bending stiffness function $D(s)$ as

$$D(s) = D_0 - \frac{D_0 - D_1}{2}\left[\tanh\frac{\gamma(s - s_0^*)}{L} - \tanh\frac{\gamma(s - s_1^*)}{L}\right], \tag{51}$$

where D_0 and D_1 denote the bending stiffness of the stiffer and softer segments, respectively, and $s \in (s_0^*, s_1^*)$ represents the softer portion arclength. Fig. 8 shows the profile of $D(s)$ in Eq. (51) with $D_1/D_0 = 0.5$, $\gamma = 200$, $s_0^*/L = 0.3$, and $s_1^*/L = 0.8$. The parameter γ is introduced to adjust the sharpness of the transition, with a larger γ resulting in a sharper stiffness transition.

To demonstrate effects of the rod inhomogeneity on the packing behavior, case studies of $D_1/D_0 = 0.001$, 0.1, and 0.5 at $s_0^*/L = 0.3$ and $s_1^*/L = 0.8$ are examined via numerical optimization. Fig. 9 shows various configurations of the constrained rod loops with the extremely soft segment of $D_1/D_0 = 0.001$. To minimize the bending energy of the entire rod, the stiffer segment adopts a configuration resembling a geodesic arc, while the softer segment undergoes more pronounced deformation to match the geometric constraint. As the rod length increases, the geodesic stiffer segment coils up ($\bar{L} > 2$), and the extremely soft segment evolves from a saddle- to a figure-eight-shaped configuration. As the total elastic energy E_{el} of the rod loop here mainly comes from the bending deformation of the stiffer segment, E_{el} is well approximated as $E_{\mathrm{el}} \approx (D_0/2)\int_0^{(s_1^*-s_0^*)L} R^{-2}\mathrm{d}s = D_0(s_1^* - s_0^*)L/(2R^2)$. This approximation is supported by numerical results which are not presented here.

In Fig. 10, we depict the configurations of the constrained rod loops with $D_1/D_0 = 0.5$. As the normalized rod length $\bar{L}$ exceeds 1, the rod loop undergoes buckling, transitioning from a great-circle- to saddle-shaped configurations. The difference in the bending stiffness between the two segments leads to the loss of $D_{2\mathrm{d}}$ symmetry and the maintenance of only mirror symmetry in the saddle-like configurations (first row in Fig. 10). In comparison with the stiffer segment, the softer segment undergoes more pronounced deformation. With a further increase in $\bar{L}$, the rod loop transforms into a figure-eight-shaped configuration, comprising two unequal ovals joined together (second row in Fig. 10), where the softer segment forms the smaller oval. At $\bar{L} = 2$, the rod loop circumscribes the great circle twice. As $\bar{L}$ continues to rise, the configurations become more complex, yet they consistently exhibit the tendency for the stiffer segment to bend less away from the great circle in comparison to the softer segment (third and fourth rows in Fig. 10). At $\bar{L} = 3$, the rod loop encircles the great circle three times. The energy profile $E_{\mathrm{el}}/(D_0/R)$ in the bottom right corner of Fig. 10 shows a similar trend to that of the homogeneous rod loop.

Fig. S6 illustrates the configurational evolution of the constrained rod loops with $D_1/D_0 = 0.1$, a pattern closely resembling that observed for $D_1/D_0 = 0.5$ in Fig. 10. The corresponding energy profile is depicted in Fig. S7. Given that $D_1/D_0 = 0.1$ in Fig. S6 falls between $D_1/D_0 = 0.001$ in Fig. 9 and $D_1/D_0 = 0.5$ in Fig. 10, the stiffer segment in Fig. S6 exhibits a bending extent away from the great circle that lies between those observed in Figs. 9 and 10.

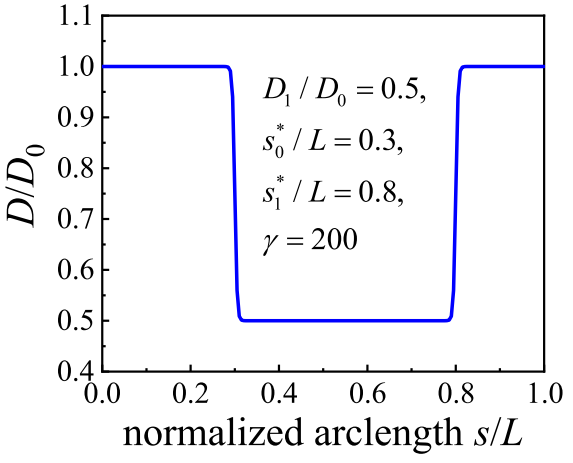

Fig. 8. Profile of the hyperbolic tangent function used to characterize the inhomogeneity of the rod bending stiffness.

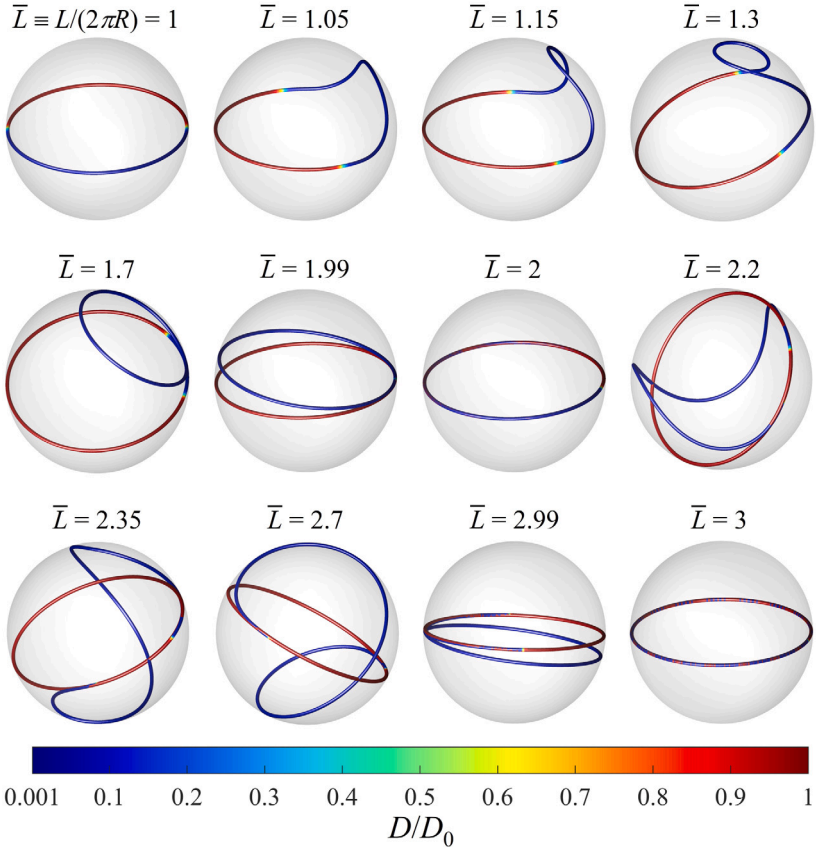

Fig. 9. Selected configurations of surface-constrained inhomogeneous rod loops with $D_1/D_0 = 0.001$, $s_0^*/L = 0.3$, and $s_1^*/L = 0.8$ at different rod lengths. The color bar indicates the distribution of $D(s)/D_0$.

6. Further discussion

This work employs the wormlike chain model for confined thin elastic rods, neglecting the twist energy. While this offers a good starting point, a more comprehensive model would include both bending and twisting components (Landau and Lifshitz, 1986; Audoly and Pomeau, 2010). For open thin rods, when the rods experience zero end-twist or the confinement does not restrict twisting, the twist energy vanishes in equilibrium (Manning, 2015). However, this does not apply to closed rod loops, necessitating further theoretical investigation into the effects of twisting on confined rod loops.

Our current analysis is restricted to rigid spherical confinement. Another important case is flexible or deformable confinement, such as elastic thin shells, biological membranes, or fluid interfaces. Packing flexible slender rods in these deformable confinement leads to mutual deformation, resulting in more complex configurations. For example, in a filament–vesicle system, depending on the relative stiffness and size of the confined filaments to vesicles, various filament configurations such as saddle, circle, oval, or twisted saddle shapes are observed (Shi et al., 2023; Zhang et al., 2024). Moreover, the deformable confinement alters system symmetry. As Figs. 5 and 6a indicate, within the rigid spherical confinement, the rod loop of normalized length $\bar{L} = 1.2$ (saddle shape with D_{2d} symmetry) shows maximum (minimum) inward-pointing contact force λ at the rod points of maximum (minimum) curvature. When replacing the rigid confinement with flexible confinement, such as a vesicle membrane, the rod expands anisotropically and the flexible confinement loses its axial symmetry. Consequently, the filament–vesicle system with a saddle-shaped filament loop exhibits C_{2v} symmetry (Shi et al., 2023), losing two axes of twofold rotational symmetry in comparison with D_{2d} symmetry of the saddle-shaped rod loop within a rigid sphere. In comparison with recent numerical simulations on the filament–vesicle morphology (Shi et al., 2023; Zhang et al., 2024), analytical predictions on the interplay between flexible rods and deformable confinement are lacking. This includes stability analysis and the shape equation at the rod–confinement contact boundary. Potential approaches might involve variational methods incorporating differential geometry and surface-based constraints.

In reality, friction between the rod and confinement may exist, hindering their relative sliding, redistributing forces along the rod, and altering the onset of rod buckling and its post-buckling behavior. Unlike the frictionless case where a normal contact force acts on the rod, frictional contact can introduce the rod to experience lateral and tangential frictional forces. Consequently, Eqs. (9) and (10) for the force and moment balance would need modifications to incorporate static or kinetic friction. Additionally, frictional contact might lead to history-dependent packing behavior, meaning the rod's configuration depends on its past interaction.

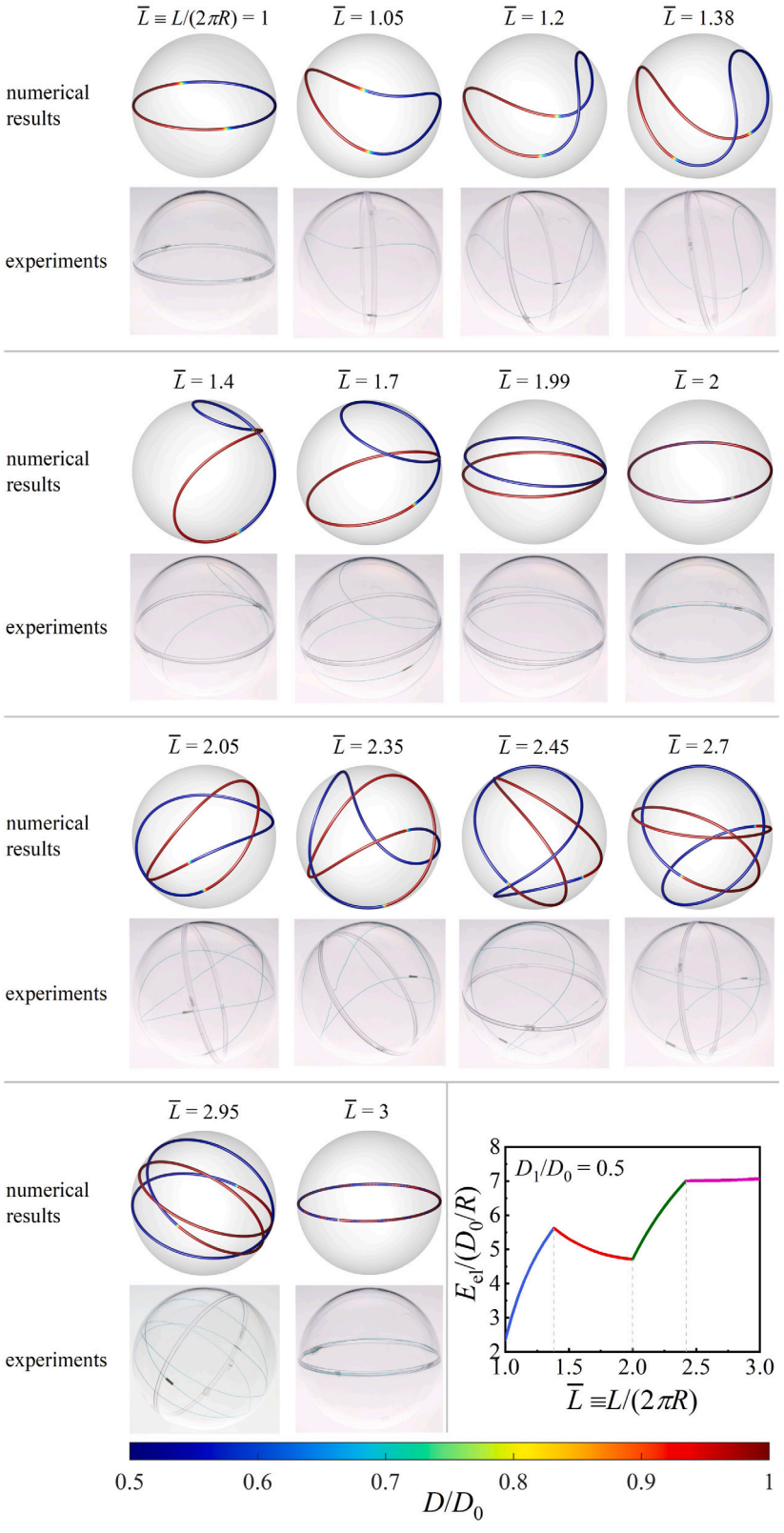

Fig. 10. Configurations and energy profile $E_{el}/(D_0/R)$ of constrained inhomogeneous rod loops with $D_1/D_0 = 0.5$, $s_0^*/L = 0.3$, and $s_1^*/L = 0.8$. Color bar, $D(s)/D_0$.

7. Conclusions

Combining analytical approaches, numerical optimization, and experimental inquiries, we study the packing behavior of thin elastic rod loops in spherical confinement, where the loop length exceeds confinement circumference. Investigating surface-constrained homogeneous rod loops yields a spectrum of stable and metastable configurations. By leveraging the Euler rotation curve approximation, formalized solutions are obtained, offering a concise yet potent means for predicting rod configurations swiftly and accurately. Various configurations such as circle, saddle, figure-eight, and more intricate patterns emerge across varying loop lengths. Based on the local balancing of force and moment, analytical solutions for rod configurations concerning internal and contact forces are also obtained, eliminating the need for analytically elusive constants of integration. Theoretical analysis on the elastic buckling of homogeneous rod loops on great circles are performed. Further numerical results indicate that the homogeneous rod loops within the spherical confinement adopt identical configurations to surface-constrained rod loops of the same lengths, thereby precluding detachment of stable rod configurations from the spherical surface. Additionally, we explore configurations of inhomogeneous rod loops comprising two stiffness segments, revealing distinct bending behavior–the stiffer segment exhibiting less deviation from the great circle, while the softer segment undergoes more pronounced deformation. The elucidation of fundamental mechanical principles governing these packing behavior holds broad relevance to filament organization within cells, cell shaping, and the fabrication of artificial cellular structures.

CRediT authorship contribution statement

Meng Wang: Formal analysis, Investigation, Methodology, Validation, Writing – original draft. **Xiying Li:** Formal analysis, Investigation, Methodology, Validation, Writing – original draft. **Xin Yi:** Conceptualization, Formal analysis, Funding acquisition, Investigation, Methodology, Supervision, Writing – review & editing.

Declaration of competing interest

The authors declare that they have no known competing financial interests or personal relationships that could have appeared to influence the work reported in this paper.

Data availability

Data will be made available on request.

Acknowledgments

This work was supported by the National Natural Science Foundation of China (12272004 and 11988102). Dr. Li thanks the experimental support from Prof. Dr. Christoph Keplinger at Max Planck Institute for Intelligent Systems. Computation resources supported by the High-performance Computing Platform of Peking University are acknowledged.

Appendix A. Curves on a surface and spherical curves

Introduce a vector function $\mathbf{S}(u_1, u_2)$ as a parametric representation of an oriented confining surface S, where u_1 and u_2 are coordinates on S. Then components of the surface metric tensor are $g_{\alpha\beta} = \mathbf{S}_{,\alpha} \cdot \mathbf{S}_{,\beta}$, where $\mathbf{S}_{,\alpha} \equiv \partial \mathbf{S}/\partial u_\alpha$ $(\alpha, \beta = 1, 2)$. The unit normal vector $\mathbf{n}_S$ to the surface S is defined as $\mathbf{n}_S = (\mathbf{S}_{,\alpha} \times \mathbf{S}_{,\beta})/\sqrt{\det g_{\alpha\beta}}$. On the surface-constrained rod curve, its unit tangent vector $\mathbf{t}$, the unit normal vector $\mathbf{n}_S$, and the unit tangent normal vector $\mathbf{g} = \mathbf{n}_S \times \mathbf{t}$ together form the Darboux frame $\{\mathbf{r}(s); \mathbf{t}(s), \mathbf{g}(s), \mathbf{n}_S(s)\}$ of the rod curve. Using orthogonality and parallelity relations of $\mathbf{t}$, $\mathbf{g}$, $\mathbf{n}_S$ and the Frenet–Serret formulas, one has (Guggenheimer, 1977)

$$\begin{pmatrix} \mathbf{t}' \\ \mathbf{g}' \\ \mathbf{n}_S' \end{pmatrix} = \begin{pmatrix} 0 & \kappa_g & \kappa_n \\ -\kappa_g & 0 & \tau_g \\ -\kappa_n & -\tau_g & 0 \end{pmatrix} \begin{pmatrix} \mathbf{t} \\ \mathbf{g} \\ \mathbf{n}_S \end{pmatrix},$$

where κ_g denotes the geodesic curvature, κ_n is normal curvature, and τ_g represents the geodesic torsion of the rod centerline curve embedded on the surface S. These three geometric parameters can be expressed as (Guggenheimer, 1977)

$$\kappa_g = \mathbf{t}' \cdot \mathbf{g} = \kappa \mathbf{n} \cdot \mathbf{g} = \kappa \cos\omega, \qquad \kappa_n = \mathbf{t}' \cdot \mathbf{n}_S = \kappa \mathbf{n} \cdot \mathbf{n}_S = -\kappa \sin\omega, \quad \text{and} \quad \tau_g = -\mathbf{n}_S' \cdot \mathbf{g} = \tau + \omega',$$

where ω denotes the angle between the unit binormal vector $\mathbf{b}$ of the rod curve and the unit normal vector $\mathbf{n}_S$ to the surface S, by which the Frenet–Serret frame $\{\mathbf{t}, \mathbf{n}, \mathbf{b}\}$ rotates around vector $\mathbf{t}$ to coincide with the Darboux frame $\{\mathbf{t}, \mathbf{g}, \mathbf{n}_S\}$. With these three expressions above, one can obtain the derivatives of κ_g, κ_n, and τ with respect to arclength s as

$$\kappa_g' = \kappa' \frac{\kappa_g}{\kappa} + \kappa_n(\tau_g - \tau), \tag{A.1}$$

$$\kappa_n' = \kappa' \frac{\kappa_n}{\kappa} - \kappa_g(\tau_g - \tau), \tag{A.2}$$

$$\tau' = \frac{-2\kappa_g \kappa_n'^2 + \kappa^2[2\kappa_g(\tau - \tau_g)^2 + \kappa_n \tau_g'] - \kappa_n^2 \kappa_g'' + \kappa_n(2\kappa_g' \kappa_n' + \kappa_g \kappa_n'')}{\kappa^2 \kappa_n}. \tag{A.3}$$

Eqs. (A.1)–(A.3) are derived based on general surfaces and can be further simplified for spherical surfaces. With the help of Eqs. (A.1)–(A.3), the internal force components F_b, F_n, and F_t given by Eqs. (17), (18), and (22), respectively, and the contact force λ in Eq. (21) can be presented as functions of κ_g for spherical surfaces (see Eqs. (24)–(27)).

Introducing the polar angle θ and the azimuthal angle ϕ in Fig. 1 (e.g., $u_1 = \theta$ and $u_2 = \varphi$), the spherical surface of radius R is parameterized as $\mathbf{S}(\theta, \varphi) = R\mathbf{e}_r(\theta, \varphi)$ with $\mathbf{e}_r$ as the surface outward unit normal vector ($\mathbf{e}_r = \mathbf{n}_S$). A spherical curve with the arclength s is parameterized as $\mathbf{r}(s) = R\mathbf{e}_r(s)$. The unit normal vector $\mathbf{e}_r$ satisfies

$$\mathbf{e}_r(s) \cdot \mathbf{e}_r(s) = 1. \tag{A.4}$$

The inextensible of the spherical curve requires $\mathbf{r}'(s) \cdot \mathbf{r}'(s) = 1$ or

$$\mathbf{e}_r'(s) \cdot \mathbf{e}_r'(s) = 1/R^2. \tag{A.5}$$

Differentiating Eq. (A.4) twice with respect to s leads to $\mathbf{e}_r'(s) \cdot \mathbf{e}_r'(s) + \mathbf{e}_r(s) \cdot \mathbf{e}_r''(s) = 0$. With Eq. (A.5), one has $\mathbf{e}_r(s) \cdot \mathbf{e}_r''(s) = -1/R^2$.

The normal curvature κ_n and the geodesic torsion τ_g of the spherical curve are, respectively,

$$\kappa_n = \mathbf{t}' \cdot \mathbf{e}_r = R\mathbf{e}_r''(s) \cdot \mathbf{e}_r(s) = -1/R \qquad \text{and} \qquad \tau_g = -\mathbf{e}_r'(s) \cdot \mathbf{g} = -\mathbf{e}_r'(s) \cdot (\mathbf{e}_r(s) \times \mathbf{t}) = -\mathbf{e}_r'(s) \cdot (\mathbf{e}_r(s) \times R\mathbf{e}_r'(s)) = 0.$$

Another relationship for a spherical curve is (Brunnett and Crouch, 1994)

$$\tau^2 \kappa^4 = \frac{(\kappa_g')^2}{R^2}.$$

Appendix B. Results for rod loops slightly deviating away from the great circle ($k^2 \ll 1$)

Recalling the relation $\mathrm{am}[4\eta \mathrm{K}(k), k] = 2\pi\eta$ and using a Maclaurin series of $\Pi(\eta; \pi/2, k)$ at $k^2 \ll 1$ as

$$\Pi(\eta; \pi/2, k) \approx \frac{\pi}{2\sqrt{1-\eta}} + \frac{\pi}{4\eta}\left(\frac{1}{\sqrt{1-\eta}} - 1\right)k^2,$$

$\varphi(L)$ from Eq. (48) is then approximated as

$$\varphi(L) \approx -\frac{\Gamma}{2cR}\left\{cL(c^2R^2-1) - 2\pi\eta(c^2R^2+1)\left[\frac{1}{\Gamma} + \frac{(c^2R^2-1)^2}{8c^2R^2}\left(1 - \frac{1}{\Gamma}\right)\right]\right\}, \tag{B.1}$$

where $\Gamma = [1 + 4k^2c^2R^2/(c^2R^2-1)^2]^{1/2}$.

At $k^2 \ll 1$, $\mathrm{K}(k) \approx \pi(1 + k^2/4)/2$ and then c given in Eq. (49) is approximated by

$$c \approx \frac{2\pi\eta}{L}\left(1 + \frac{k^2}{4}\right). \tag{B.2}$$

Substituting Eq. (B.2) into Eq. (B.1), a Maclaurin series of $\varphi(L)$ with terms of k up to degree 2 in Eq. (B.1) reads

$$\varphi(L) \approx -\frac{L}{R}\mathrm{sgn}(\bar{L} - \eta) - \frac{L\eta^2}{R|\bar{L}^2 - \eta^2|}k^2. \tag{B.3}$$

Recalling $\varphi(L) = 2\pi p$ in Eq. (50), from Eq. (B.3) one has

$$k^2 = -\frac{(\bar{L}^2 - \eta^2)}{\bar{L}\eta^2}[\bar{L} + p\,\mathrm{sgn}(\bar{L} - \eta)]. \tag{B.4}$$

In cases where the constrained rod has a slight deviation away from the great circle, k^2 is small. Fig. 11 shows that in these cases Eq. (B.4) agrees well with the fully nonlinear solutions obtainable through numerical evaluation using Eq. (50).

Substituting Eq. (B.4) into Eq. (49), parameter c can be analytically obtained, and then geometric properties such as κ and τ and contact force λ can be directly accessed using Eqs. (36) and (38), respectively. Again, in cases where the confined rod slightly deviates away from the great circle, κ, τ, and λ based on k^2 given by Eq. (B.4) agree well with the fully nonlinear solutions (Fig. S8).

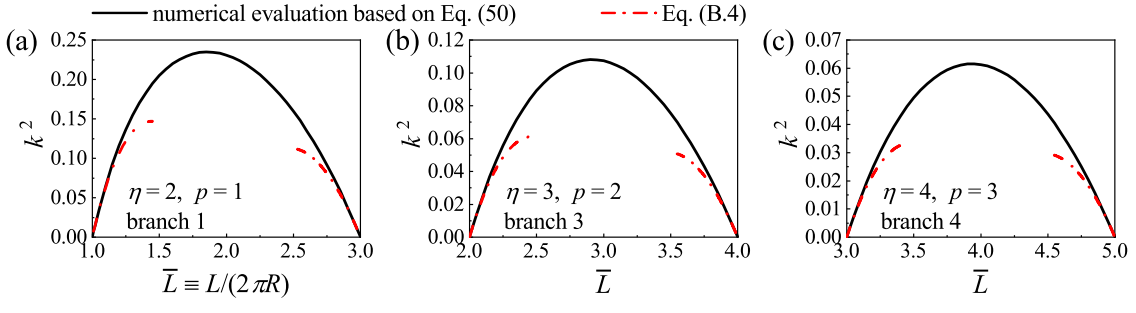

Fig. 11. k^2 versus $\bar{L}$ at selected sets of (η, p). Solid lines, numerical evaluation based on Eq. (50); dash-dotted lines, Eq. (B.4).

Appendix C. Supplementary data

Supplementary material related to this article can be found online at https://doi.org/10.1016/j.jmps.2024.105771.

References

Arroyo, J., Garay, O.J., Mencía, J., 2006. Elastic circles in 2-spheres. J. Phys. A: Math. Gen. 39, 2307–2324.

Audoly, B., Pomeau, Y., 2010. Elasticity and Geometry: From Hair Curls to the Non-linear Response of Shells. Oxford University Press, Oxford, UK.

Bohle, C., Peters, G.P., Pinkall, U., 2008. Constrained Willmore surfaces. Calc. Var. Partial Differ. Equ. 32, 263–277.

Boresi, A.P., 1955. A refinement of the theory of buckling of rings under uniform pressure. J. Appl. Mech. 22, 95–102.

Boué, L., Adda-Bedia, M., Boudaoud, A., Cassani, D., Couder, Y., Eddi, A., Trejo, M., 2006. Spiral patterns in the packing of flexible structures. Phys. Rev. Lett. 97, 166104.

Brunnett, G., Crouch, P.E., 1994. Elastic curves on the sphere. Adv. Comput. Math. 2, 23–40.

Chen, C., Zhang, T., 2022. Coupling lattice model and many-body dissipative particle dynamics to make elastocapillary simulation simple. Extreme Mech. Lett. 54, 101741.

Chwalla, E., Kollbrunner, C.F., 1938. Beiträge zum Knickproblem des Bogenträgers und des Rahmens. Der Stahlbau 11, 73–78.

Coshic, K., Maffeo, C., Winogradoff, D., Aksimentiev, A., 2024. The structure and physical properties of a packaged bacteriophage particle. Nature 627, 905–914.

Diagouraga, B., Grichine, A., Fertin, A., Wang, J., Khochbin, S., Sadoul, K., 2014. Motor-driven marginal band coiling promotes cell shape change during platelet activation. J. Cell Biol. 204, 177–185.

Dmitrieff, S., Alsina, A., Mathur, A., Nédélec, F.J., 2017. Balance of microtubule stiffness and cortical tension determines the size of blood cells with marginal band across species. Proc. Natl. Acad. Sci. USA 114, 4418–4423.

Doi, M., Edwards, S.F., 1986. The Theory of Polymer Dynamics. Oxford University Press, Oxford, UK.

Farin, G., 2002. Curves and Surfaces for CAGD: A Practical Guide, fifth ed. Morgan Kaufmann, San Francisco, USA.

Fletcher, R., 1987. Practical Methods of Optimization, second ed. John Wiley & Sons, Ltd., Chichester, UK.

Geppert, H., 1941. Sopra una caratterizzazione della sfera. Ann. Mat. 20, 59–66.

Ghomi, M., 2019. Torsion of locally convex curves. Proc. Amer. Math. Soc. 147, 1699–1707.

Graham, K., Chandrasekaran, A., Wang, L., Yang, N., Lafer, E.M., Rangamani, P., Stachowiak, J.C., 2024. Liquid-like condensates mediate competition between actin branching and bundling. Proc. Natl. Acad. Sci. USA 121, e2309152121.

Guggenheimer, H.W., 1977. Differential Geometry. Dover Publications, New York, USA.

Guven, J., Vázquez-Montejo, P., 2012. Confinement of semiflexible polymers. Phys. Rev. E 85, 026603.

Heller, L., 2014. Constrained Willmore tori and elastic curves in 2-dimensional space forms. Comm. Anal. Geom. 22, 343–369.

Huang, W.-Z., Li, B., Feng, X.-Q., 2024. Mechanobiological tortuosity of blood vessels with stress-modulated growth and remodeling. J. Mech. Phys. Solids 186, 105605.

Huynen, A., Detournay, E., Denoel, V., 2016. Surface constrained elastic rods with application to the sphere. J. Elasticity 123, 203–223.

Jiang, H., Sun, S.X., 2010. Morphology, growth, and size limit of bacterial cells. Phys. Rev. Lett. 105, 028101.

Kratky, O., Porod, G., 1949. Röntgenuntersuchung gelöster Fadenmoleküle. Recl. Trav. Chim. Pays-Bas 68, 1106–1122.

Landau, L.D., Lifshitz, E.M., 1986. Theory of Elasticity, third ed. Butterworth-Heinemann, New York, USA.

Langer, J., Singer, D.A., 1984. The total squared curvature of closed curves. J. Differ. Geom. 20, 1–22.

Limozin, L., Sackmann, E., 2002. Polymorphism of cross-linked actin networks in giant vesicles. Phys. Rev. Lett. 89, 168103.

Lombardo, F., Goriely, A., Napoli, G., 2018. Asymmetric equilibria of two nested elastic rings. Mech. Res. Commun. 94, 91–94.

Manning, G.S., 2015. The energy of naturally curved elastic rods with an application to the stretching and contraction of a free helical spring as a model for DNA. J. Chem. Phys. 143, 104901.

Millman, R.S., Parker, G.D., 1977. Elements of Differential Geometry. Prentice-Hall, Englewood Cliffs, USA, p. 170.

Pinkall, U., 1985. Hopf tori in S^3. Invent. Math. 81, 379–386.

Purohit, P.K., Kondev, J., Phillips, R., 2003. Mechanics of DNA packaging in viruses. Proc. Natl. Acad. Sci. USA 100, 3173–3178.

Rogers, D.F., Adams, J.A., 1990. Mathematical Elements for Computer Graphics, second ed. McGraw-Hill, New York, USA, p. 250.

Sannyamath, S., Vetter, R., Bonart, H., Hartmann, M., Ganguly, R., Hardt, S., 2024. Disorder-to-order transition of long fibers contained in evaporating sessile drops. Soft Matter 20, 3107–3117.

Shaebani, M.R., Najafi, J., Farnudi, A., Bonn, D., Habibi, M., 2017. Compaction of quasi-one-dimensional elastoplastic materials. Nature Commun. 8, 15568.

Shi, C., Zou, G., Wu, Z., Wang, M., Zhang, X., Gao, H., Yi, X., 2023. Morphological transformations of vesicles with confined flexible filaments. Proc. Natl. Acad. Sci. USA 120, e2300380120.

Singer, J., Babcock, C.D., 1970. On the buckling of rings under constant directional and centrally directed pressure. J. Appl. Mech. 37, 215–218.

Slesarenko, V., Rudykh, S., 2017. Microscopic and macroscopic instabilities in hyperelastic fiber composites. J. Mech. Phys. Solids 99, 471–482.

Stoop, N., Najafi, J., Wittel, F.K., Habibi, M., Herrmann, H.J., 2011. Packing of elastic wires in spherical cavities. Phys. Rev. Lett. 106, 214102.

Thorbergsson, G., Umehara, M., 1999. A Unified Approach to the Four Vertex Theorems. II, Differential and Symplectic Topology of Knots and Curves. In: Amer. Math. Soc. Transl. Ser. 2, vol. 190, Amer. Math. Soc., Providence, RI, pp. 229–252.

Timoshenko, S.P., Gere, J.M., 1961. Theory of Elastic Stability. McGraw-Hill Book Company, New York, USA.

Tsai, F.-C., Koenderink, G.H., 2015. Shape control of lipid bilayer membranes by confined actin bundles. Soft Matter 11, 8834–8847.

Vetter, R., Wittel, F.K., Herrmann, H.J., 2014. Morphogenesis of filaments growing in flexible confinements. Nature Commun. 5, 4437.

Wang, M., Yi, X., 2024. Equilibrium analysis of surface-constrained elastic rods: Unveiling contact and internal forces through local geometry. J. Mech. Phys. Solids 187, 105635.

Zhang, C., Fang, Y., Shi, C., Yuan, H., Yi, X., 2024. Stretching transition of vesicles with confined filament loops: Morphological evolution with filament distortion and reorientation. Giant 17, 100233.

Zou, G., Yi, X., Zhu, W., Gao, H., 2018. Packing of flexible nanofibers in vesicles. Extreme Mech. Lett. 19, 20–26.

Supplementary materials for

"Deformation, shape transformations, and stability of elastic rod loops within spherical confinement"

Meng Wang, Xiying Li, Xin Yi

State Key Laboratory for Turbulence and Complex System, Department of Mechanics and Engineering Science,

College of Engineering, Peking University, Beijing 100871, China

Note 1. Experiments

The rigid spherical confinement in Fig. 2 within the main text consists a commercially available transparent Acrylic spherical shell comprising two hemispherical parts, each with a radius of 4 cm. The elastic rod loops are commercial Nylon fishing lines, treated as inextensible due to the high Young's modulus around 2.7 GPa. For homogeneous rod loops, the fishing lines have a diameter of 0.47 mm. In the case of two-phase inhomogeneous rod loops with a bending stiffness ratio of 0.5, the stiffer segment has a diameter of 0.32 mm and the softer segment has a diameter of 0.27 mm. For two-phase inhomogeneous rod loops with a bending stiffness ratio of 0.1, the stiffer portion has a diameter of 0.27 mm and the softer portion has a diameter of 0.15 mm. The fishing lines are pre-stretched overnight to ensure a straight initial state. The fishing lines of prescribed lengths are connected using glue to form the elastic loops, which are then packed into the spherical shells. Equilibrium configurations of the confined rod loops could be achieved by gently shaking the Acrylic shells, if necessary.

Note 2. Supplementray numerical results for homogeneous rod loops

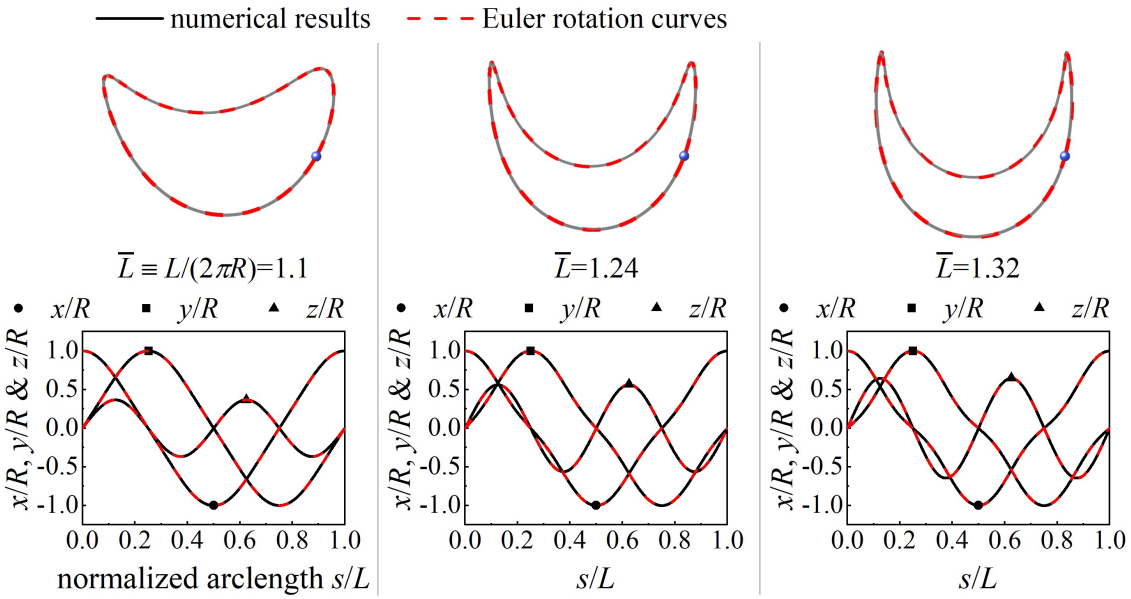

Figure S1. Comparison of configurations and corresponding coordinates between numerical optimization results and the Euler rotation curve approximations with $l = 2$ at the rod length $\bar{L} \equiv L/(2\pi R) = 1.1$, 1.24, and 1.32. The locations with $s = 0$ is designated by blue dots in the rod configurations.

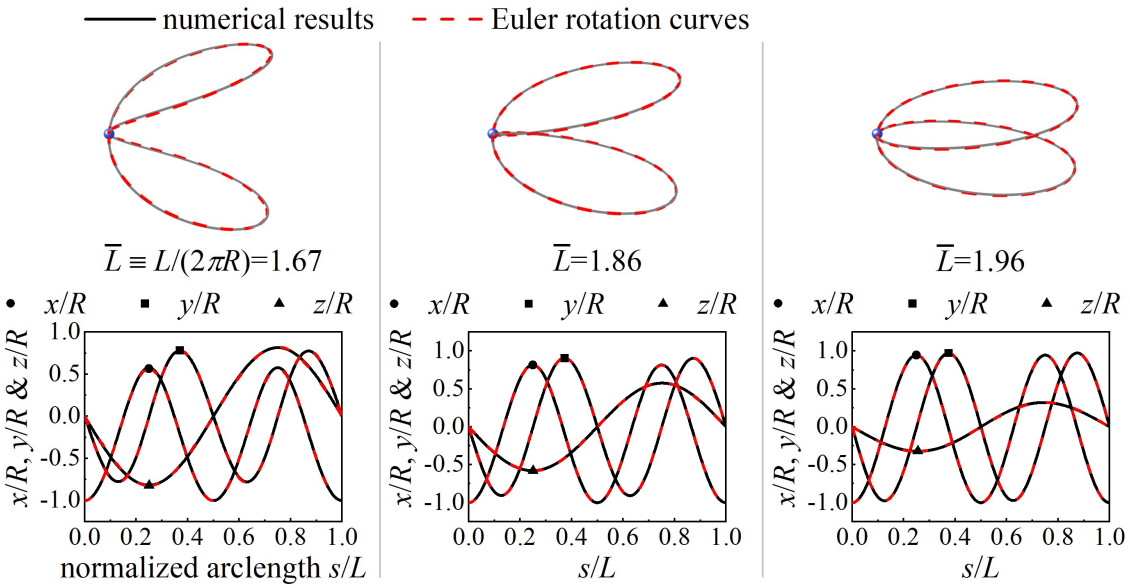

Figure S2. Comparison of configurations and corresponding coordinates between numerical optimization results and Euler rotation curve approximations with $l = 1$ at the rod length $\bar{L} \equiv L/(2\pi R) = 1.67$, 1.86, and 1.96. Blue dots, $s = 0$.

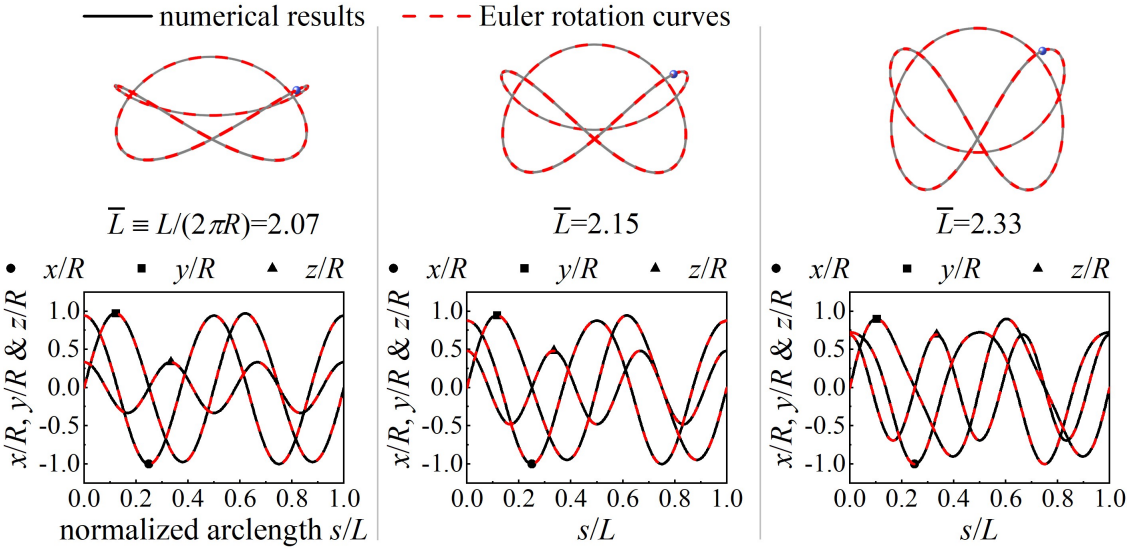

Figure S3. Comparison of configurations and corresponding coordinates between numerical optimization results and Euler rotation curve approximations with $l = 3$ at the rod length $\bar{L} \equiv L/(2\pi R) = 2.07$, 2.15, and 2.33. Blue dots, $s = 0$.

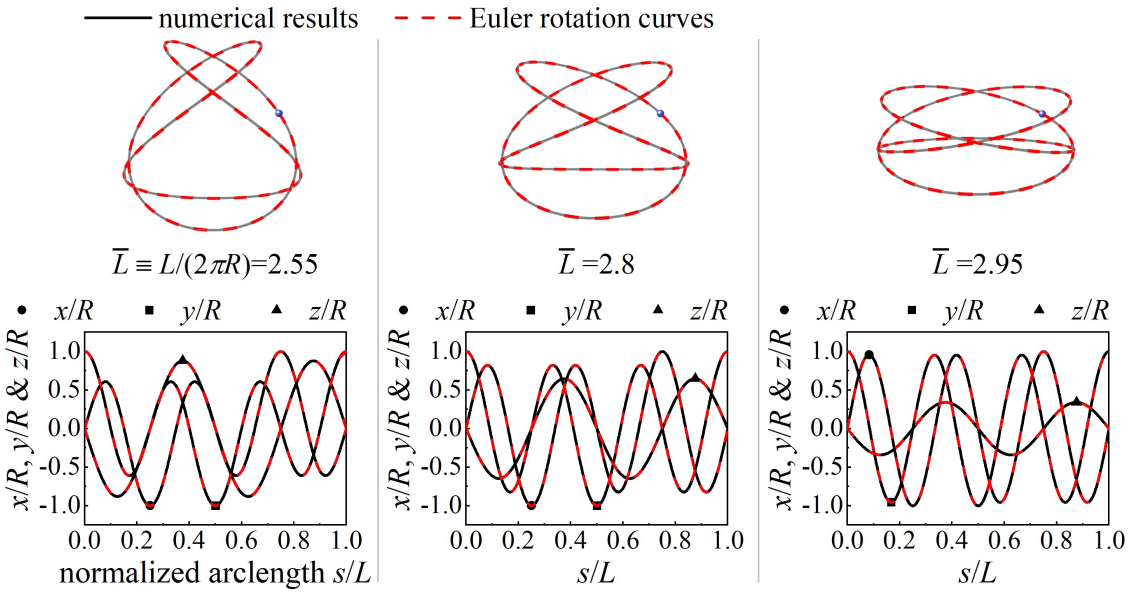

Figure S4. Comparison of configurations and corresponding coordinates between numerical optimization results and Euler rotation curve approximations with $l = 2$ at the rod length $\bar{L} \equiv L/(2\pi R) = 2.55$, 2.8, and 2.95. Blue dots, $s = 0$.

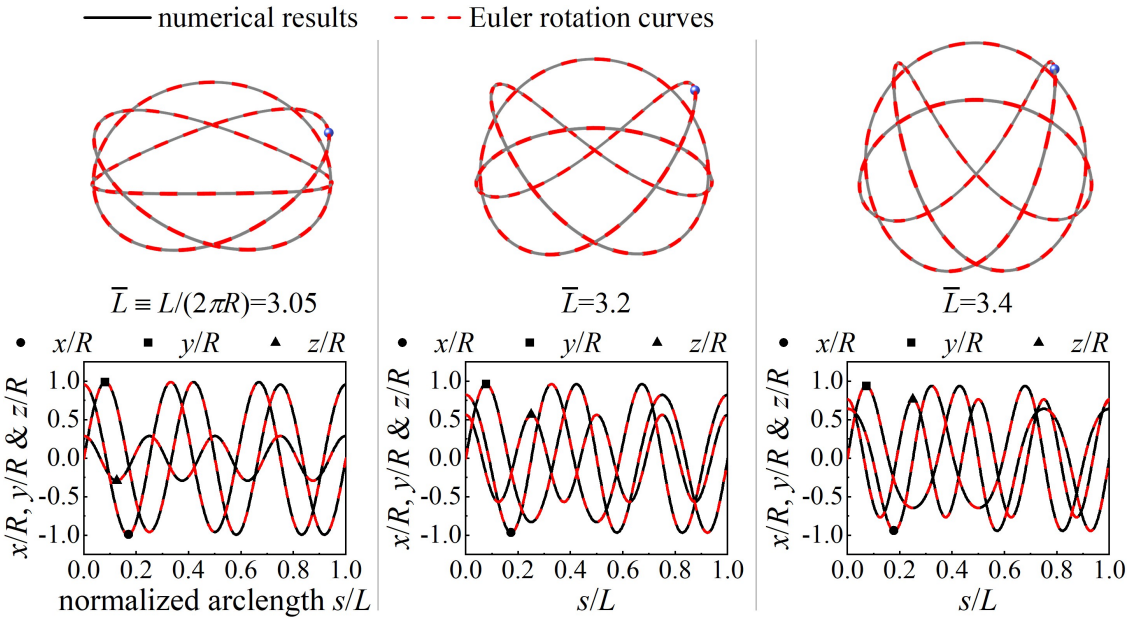

Figure S5. Comparison of configurations and corresponding coordinates between numerical optimization results and Euler rotation curve approximations with $l = 4$ at the rod length $\bar{L} \equiv L/(2\pi R) = 3.05$, 3.2, and 3.4. Blue dots, $s = 0$.

Note 3. Supplementray numerical results for inhomogeneous rod loops

The confined inhomogeneous rod loop comprises a softer segment and a stiffer segment. whose bending stiffness distribution can be described by Eq. (51) in the main text. In Eq. (51), D_0 and D_1 denote the bending stiffness of the stiffer and softer segments, respectively, and $s \in (s_0^*, s_1^*)$ represents the softer portion arclength. Fig. S6 shows configurations of confined inhomogenous rod loops with $D_1/D_0 = 0.1$, $s_0^*/L = 0.3$ and $s_1^*/L = 0.8$, and the corresponding energy profile is depicted in Fig. S7.

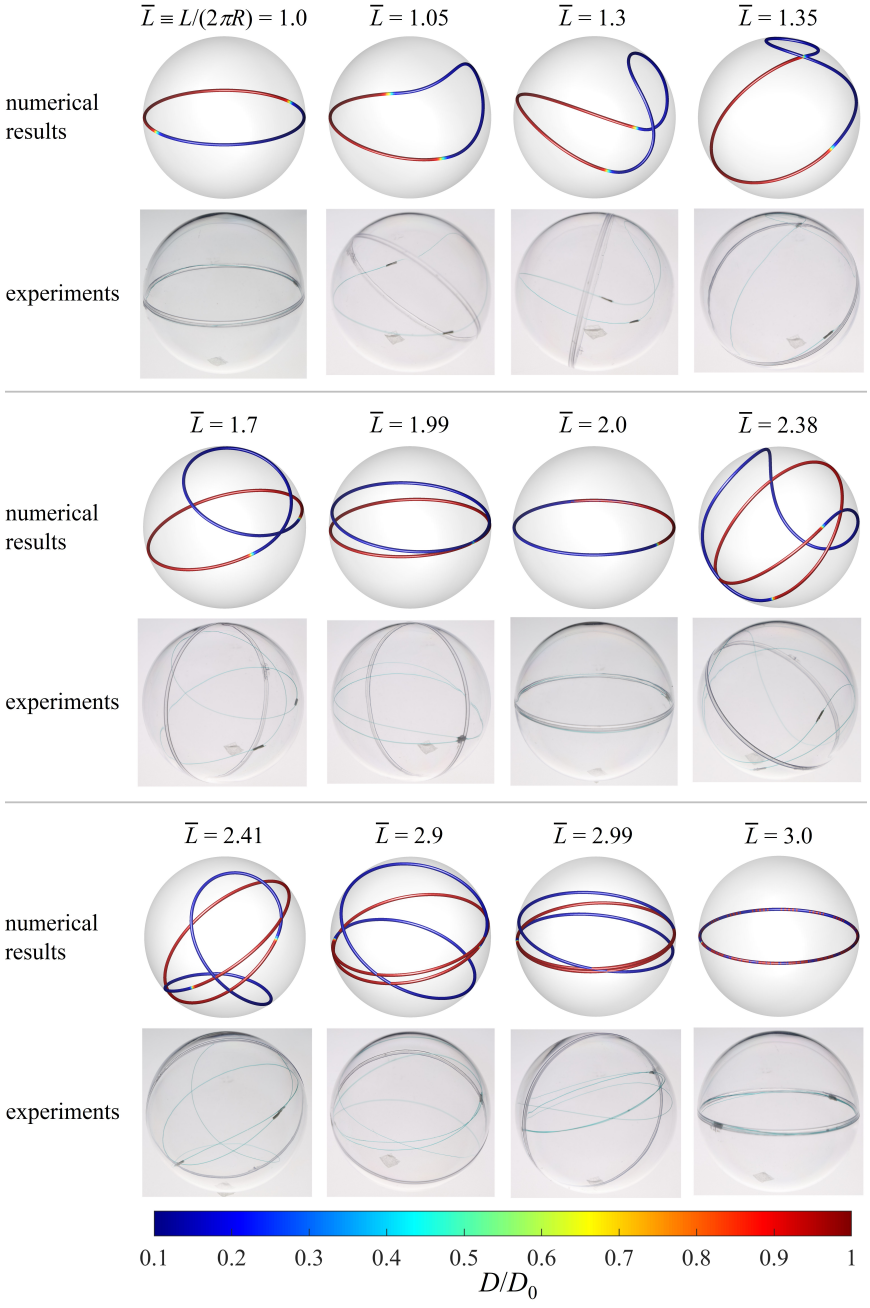

Figure S6. Configurations of confined inhomogeneous rod loops of $D_1/D_0 = 0.1$, $s_0^*/L = 0.3$ and $s_1^*/L = 0.8$ at different rod lengths. Color bar, $D(s)/D_0$.

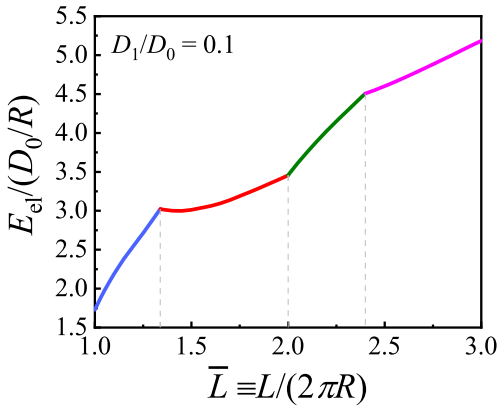

Figure S7. Energy profile $E_{el}/(D_0/R)$ of the stable configurations of the confined inhomogeneous rod loops with $D_1/D_0 = 0.1$, $s_0^*/L = 0.3$ and $s_1^*/L = 0.8$.

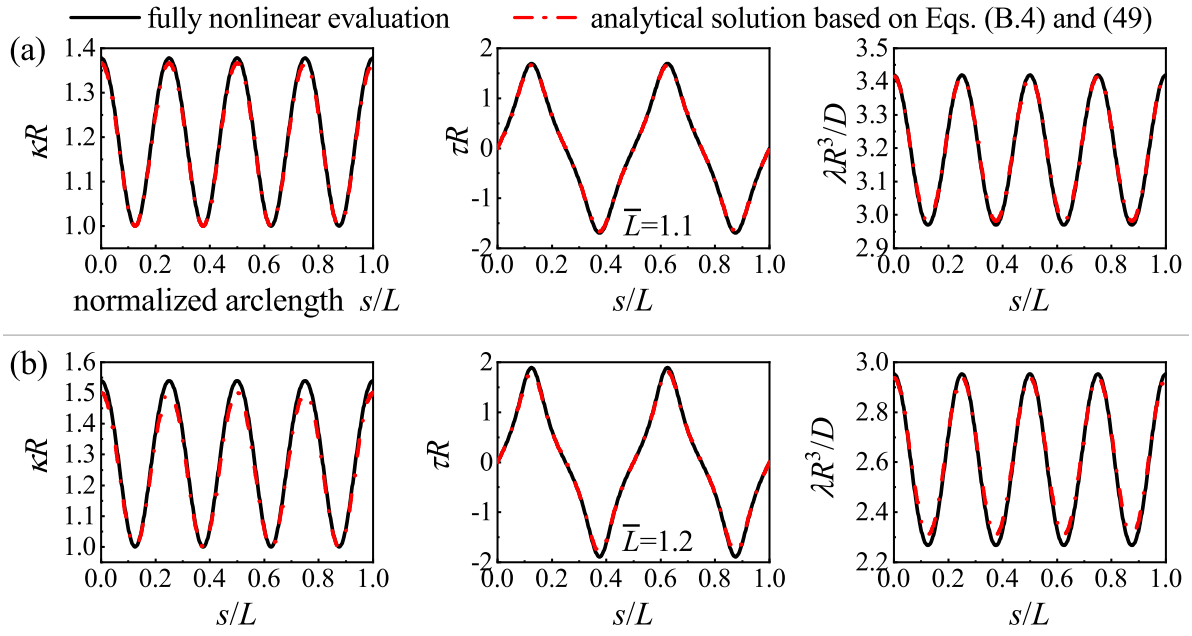

Figure S8. Normalized curvature κR, torsion τR, and contact force $\lambda R^3/D$ versus the normalized arclength s/L at (a) and 1.2 (b). Here $\eta = 2$ and $p = 1$ in branch 1 are taken.